AN ABSTRACT OF THE THESIS OF

William C. Koski for the degree of Master of Science in Mechanical Engineering presented on September 6, 2012

Title: Design, Analysis, and Validation of Composite C-Channel Beams

Abstract approved:

_____

John P. Parmigiani

A lightweight carbon fiber reinforced polymer (CFRP) c-channel beam was previously designed using analytical theory and finite element analysis and subsequently manufactured through a pultrusion process. Physical testing revealed the prototype did not meet the bending and torsional stiffness of the beam model. An investigation revealed that the manufactured prototype had lower fiber content than designed, compacted geometry, an altered ply layup, missing plies, and ply folds. Incorporating these changes into the beam model significantly improved model-experiment agreement.

Using what was learned from the initial prototype, several new beam designs were modeled that compare the cost per weight-savings of different composite materials. The results of these models show that fiberglass is not a viable alternative to CFRP when designing for equivalent stiffness. Standard modulus carbon was shown

to have slightly lower cost per-weight savings than intermediate modulus carbon, although intermediate modulus carbon saves more weight overall. Core materials, despite potential weight savings, were ruled out as they do not have the crush resistance to handle the likely clamp loads of any attaching bolts. Despite determining the ideal materials, the manufactured cost per weight-savings of the best CFRP beam design was about double the desired target.

Design, Analysis, and Validation of Composite C-Channel Beams

by
William C. Koski

A THESIS

submitted to

Oregon State University

in partial fulfillment of
the requirements of the
degree of

Master of Science

Presented September 6, 2012
Commencement June 2013

Master of Science thesis of William C. Koski presented on September 6, 2012.

APPROVED:

Major Professor, representing Mechanical Engineering

Head of the School of Mechanical, Industrial, and Manufacturing Engineering

Dean of the Graduate School

I understand that my thesis will become part of the permanent collection of Oregon State University libraries. My signature below authorizes release of my thesis to any reader upon request.

William C. Koski, Author

ACKNOWLEDGEMENTS

I would like to express my sincere gratitude to my advisor Dr. John Parmigiani. His guidance during my undergraduate senior year was my primary reason for pursuing a graduate degree at Oregon State University. Completion of my degree would not have been possible without his support, enthusiasm, and the opportunity he provided me.

I would also like to thank my committee members Dr. Brian Bay and Dr. Roberto Albertani for their input and assistance throughout my graduate research.

My thanks also go out to Mark Locatelli, Justin Yee, Barry Outen, and Todd Gilbert for working with me, supporting me, and acting as excellent resources during my research.

Finally, I must thank my friends, family, and fellow graduate students for their ongoing encouragement and motivation. They helped make graduate school a fulfilling and enjoyable experience.

TABLE OF CONTENTS

TABLE OF CONTENTS (Continued)

Page

TABLE OF CONTENTS (Continued)

Page

LIST OF FIGURES

Figure Page

LIST OF FIGURES (Continued)

Figure Page

LIST OF TABLES

LIST OF TABLES (Continued)

Table Page

LIST OF APPENDIX FIGURES

Figure Page

Design, Analysis, and Validation of Composite C-Channel Beams

1 Introduction

1.1 Background and Motivation

Composite materials are commonly used as lightweight alternative materials to metals in structural applications due to their high strength and stiffness per weight. This reduction in weight can lead to performance and fuel efficiency increases in transportation applications including aircraft, boats, and road vehicles.

Ideally, structures using composites should be designed to utilize the manufacturability advantages of composites; however, this is not always possible. Such composite manufacturability advantages include the ability to form into complex shapes, which can lead to the consolidation of several parts into one. However, when trying to reduce the weight of existing metal structures, it is necessary to design composite parts as drop-in replacements for their metal counterparts. Doing so requires the composite part to match the mechanical properties of the corresponding metal part. This thesis explores the mechanical and economic feasibility of a composite drop-in replacement for a structural steel c-channel beam.

1.2 Fiber Reinforced Composites Overview

A composite material is one made up of multiple different constituent materials that performs better than any of the constituent materials alone. In the case of fiber reinforced composites, it is a compliant matrix material reinforced with strong and

stiff fibers. The resulting material is stronger and stiffer than the matrix material alone, and the matrix binds the fibers together allowing them to take transverse and compressive loads. Typical matrix materials include polymers such as epoxy, polyester, and vinylester. Common fiber reinforcements include carbon (also known as graphite), aramid, and glass.

Fiber reinforced polymers (FRP) have several advantages over conventional materials such as plastics and metals. Polymers have the ability to form into complex shapes, allowing FRPs to achieve geometry that may not be possible with metals. FRPs also tend to have better corrosion resistance than metals, provided that the matrix material sufficiently coats and protects the fibers from environmental effects. Many FRPs, especially carbon fiber reinforced polymers (CFRP) and boron reinforced polymers, have a higher specific strength and specific stiffness in the fiber direction than metals such aluminum and steel [1].

In order to handle loads in more than one direction, it becomes necessary to orient fibers in multiple directions. This can be done by chopping up fibers and orienting them randomly, weaving fibers together, or stitching fibers together in two or more directions. It can also be done by creating a stack of unidirectional layers and orienting the layers to handle the applied loads. Each layer is known as a ply, or lamina, and the completed stack is known as a laminate.

The orthotropic nature of unidirectional plies requires more material property definitions than isotropic materials such as metals. There are four in-plane properties necessary to define a lamina. They are the elastic modulus in the fiber direction ($E11$),

the elastic modulus in the transverse direction ($E22$), the in-plane shear modulus ($G12$) and the major Poisson's ratio ($\nu 12$). The material coordinate system will be expanded upon in section 2.1.

1.3 Literature Review

There is extensive literature covering the use of lightweight composite materials to make structural beams. This section reviews studies on FRP reinforced metal beams, fully composite beams, and a comparison of materials in composite beams.

1.3.1 FRP Reinforced Metal Beams

FRP has been studied as a light weight material for reinforcing metal beams. This is one possible way to increase the stiffness and strength per weight of c-channel beams.

A 1977 study observed the effects of reinforcing steel c-channel beams with bonded CFRP strips [2]. The study showed that using CFRP instead of steel to reinforce the beams could reduce the weight of the reinforcement strip by a factor of 10, although a different reinforcement shape was also used. A scaled down prototype was built and tested to show increased bending stiffness, increased failure load, and fatigue tolerance over 500,000 loading cycles. Although the study showed successful use of FRP reinforcing strips, the author recommends further testing to determine the strips resistance to environmental degradation.

A similar 1997 study looked at the behavior of CFRP reinforced aluminum extruded box beams. Unidirectional strips of CFRP were bonded to the bottom flange of aluminum box beams with fibers oriented along the length of the beam [3]. Four-

point bend testing showed that the reinforced beams had 75% higher stiffness, 63% higher ultimate strength, and only 7% more weight than the non-reinforced aluminum beams. These results agreed with simple analytical theory. However, the study did not look at fatigue performance, which would be a critical in determining if the CFRP strip would remain bonded to the aluminum beam.

An analytical study of rectangular cross-section steel beams reinforced with CFRP plates was published in 2004 [4]. It looked at the stress concentration where the bonded CFRP plate terminates under mechanical and thermals loads. Tapering the ends of the CFRP plate reduced the stress concentration, and the analytical findings were validated by a finite element model. Again, the model does not consider the fatigue strength of the adhesive which would be necessary if applied to a beam. Experimental validation would have also been useful.

These studies show that FRP can be used as a lightweight reinforcement for metal beams; however, this method does not achieve the weight savings that a fully FRP beam would. The bonding issue between the FRP reinforcement strip and the metal beam also remains an issue under fatigue loading and environmental degradation.

1.3.2 Fully Composite Beams

There is extensive literature on the design, manufacture, and experimental validation of fully composite beams of various cross-sectional shapes. In 1989 Bank used Timoshenko and Euler-Bernoulli beam theories to predict the flexural and shear moduli of thin walled glass fiber reinforced polymer (GFRP) pultruded I-beams and

validated them with experiments [5]. A 1995 study by Brooks and Turvey used analytical theory and FEA to predict buckling loads of pultruded GFRP I-beams; however, model-experiment discrepancies suggested that initial deflections and pre-buckling deformations needed to be considered in the models [6]. In 1996 Davalos et. al. used FEA and a lamination theory based computer program to predict the bending behavior of GFRP H-beams and box beams, which were validated with experiments [7]. A 1997 study by Davalos and Qiao predicted the lateral-distortional and flexural-torsional response of pultruded FRP wide-flange beams using non-linear elastic theory, and the predictions were validated with experiments and finite element (FE) models [8]. A similar study in 2005 by Shan and Qiao used analytical and FE methods to predict flexural-torsional buckling behavior of pultruded FRP c-channel beams, which was also validated with experiments [9]. A 2006 study by Zhou and Hood explored the use of a hot press and open mold to fabricate CFRP I-beams [10]. Experimental testing agreed well with analytical predictions despite manufacturing defects such as flange-web joint issues and ply discontinuities.

Although most of these studies reached good agreement between the models and experiments, they lacked information in key areas. The papers do not discuss weight savings of the beams when compared to steel beams of equivalent stiffness or strength. They also do not mention the manufacturing costs, although many of them used a pultrusion method – a lower cost, higher volume manufacturing method. Together, this information could be used to determine the cost per weight-savings of a FRP beam compared to a steel beam.

1.3.3 Comparison of Composite Materials in Beams

In 1997 Kim compared the performance and cost of aluminum, FRP, and aluminum-FRP hybrid beams [11]. He did so by designing equivalently stiff, weight-optimized box beams from each material and comparing their resulting weight and costs. He repeated this process for box beams with equivalent strength. The aluminum box beam featured a profile with thicker flanges and thinner webs to maximize bending stiffness per weight. The aluminum-FRP hybrid beam used a similar aluminum profile but with unidirectional FRP bonded to the top and bottom flanges to increase bending stiffness. The FRP beam had webs made primarily of angle-ply layers to resist shear deformation and flanges with unidirectional plies to resist bending. Kim concluded that a fully CFRP beam yielded the greatest weight savings. GFRP was quickly eliminated as a possible material when designing for low weight since it is heavier than aluminum when designing for equivalent stiffness. Kim showed that a CFRP beam will yield up to a 60% weight savings compared to aluminum, and that the aluminum-CFRP beam will save up to 40% in weight, when designed for equivalent stiffness. The CFRP beam cost $31.02 per kg of weight saved, and the aluminum-CFRP hybrid cost $29.53 per kg saved compared to the aluminum beam. However, Kim mentions that the cost estimations could vary greatly depending on manufacturing method and production volume. He also suggests further analysis of the bonding between the CFRP and aluminum of the hybrid beam.

This study is useful for considering composite materials for structural c-channel beams. The material analysis and comparison of metal-FRP hybrid and fully

FRP beams can guide material selection for beams despite the differing cross-sectional shapes. The only aspect that was lacking from the study was physical validation of the beam designs.

1.4 Prototype-A Beam Design

A CFRP prototype beam, referred to as prototype-A, was previously designed as part of this project. This section will review the design of the prototype-A beam which includes the stiffness targets, materials used, and ply layup.

1.4.1 Stiffness Targets

The prototype-A beam was designed to meet certain vertical bending, lateral bending, and torsional stiffness values. Bending stiffness is reported in terms of the effective elastic modulus, E, multiplied by the second moment of area, I. However, vertical bending stiffness is reported as an "effective" bending stiffness, which combines deflection due to bending as well as shear. Since bending deflection depends on the length of the beam cubed, and shear deflection depends on the length, the effective vertical bending stiffness is only valid for a particular length. Torsional stiffness is reported in terms of effective shear modulus, G, multiplied by the polar moment of inertia, J. Vertical and lateral bending stiffnesses are the beam's resistance to a vertical force, F_Z, and lateral force, F_Y, respectively. Torsional stiffness is the beam's resistance to a torque, T_X. These loads are shown on the beam in Figure 1, and the stiffness targets are shown in Table 1.

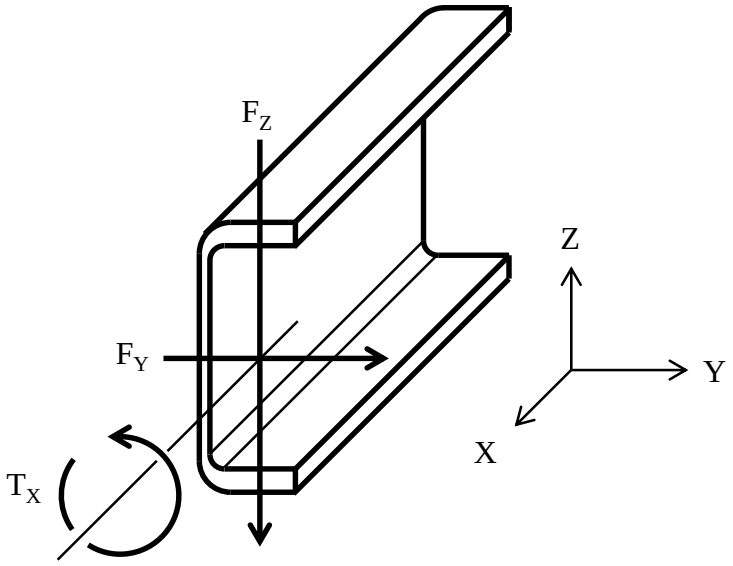

Figure 1 Load diagram for prototype-A beam

Table 1 Bending stiffness targets for prototype-A beam

Effective $EI_{vertical}$ ($lbs*in^2$)	**$EI_{lateral}$ ($lbs*in^2$)**	**$GJ_{torsional}$ ($lbs*in^2$)**
2.46E+09	1.43E+08	1.60E+06

1.4.2 Materials

The prototype-A beam was designed with two material types in three different configurations. Intermediate modulus (IM) carbon fibers were stitched to a thin chopped mat backing to form a 0° unidirectional (UD) fabric, with fibers running along the length of the beam. IM carbon fibers were also used in a non-stitched 0° tow configuration. Standard modulus (SM) carbon fibers were stitched together in a triaxial (TA) configuration made up of 45, -45, and 90° plies.

Composite material properties were estimated for each fiber type. This was done using the rule of mixtures (ROM), which combines material properties of each

fiber type with material properties for structural epoxy based on the ratio of fiber to epoxy. The weight fraction of fiber (W_f), in this case, was 72.4%. The IM unidirectional fabric and tow were estimated to have the same properties as each other. The triaxial fabric was broken down and modeled as three separate plies of unidirectional SM CFRP. The composite material properties for unidirectional IM and SM CFRP are shown in Table 2.

Table 2 Estimated material properties for IM and SM unidirectional CFRP using ROM

Material Type	W_f	E11 (psi)	E22 (psi)	G12 (psi)	v12
IM UD CFRP	72.4%	2.80E+07	1.28E+06	6.16E+05	0.253
SM UD CFRP	72.4%	2.19E+07	1.16E+06	6.16E+05	0.253

1.4.3 Ply Layup

The prototype-A beam ply layup was designed to maximize stiffness and minimize weight. This was achieved by placing the majority of the IM unidirectional fabric in the flange centers to maximize vertical bending stiffness. IM unidirectional tow was placed in radius transition in order to make a smooth change from the thinner web to thicker flange. Additional plies of IM unidirectional fabric are located along the entire perimeter which adds to both vertical and lateral bending stiffness. SM triaxial fabric was also placed along the entire perimeter to maximize torsional stiffness. The layup in the web is $\left[\text{IM-UD/SM-TA}_3\text{/IM-UD/SM-TA}\right]_S$ and the layup in the flange is $\left[\text{IM-UD/SM-TA}_3\text{/IM-UD/SM-TA/}\overline{\text{IM-UD}_{17}}\right]_S$. A simplified version of this layup is shown in Figure 2.

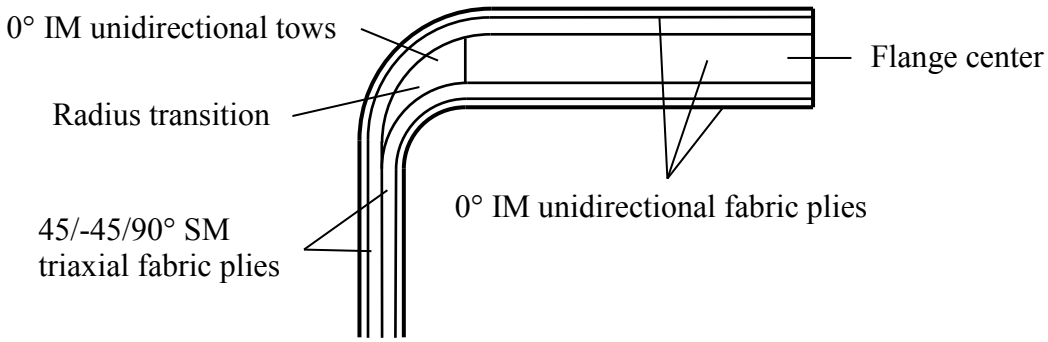

Figure 2 Diagram of prototype-A simplified ply layup

1.5 Thesis Scope

This thesis will cover the gaps discussed in the previous literature and extend the work of the prototype-A beam. Although each of the previous papers contributed important aspects of using composites for lightweight structural beams, none of them considered the entire process of material selection, design, physical validation, and cost modeling. This thesis covers the finite element (FE) modeling of the prototype-A beam and the experimental results of the manufactured prototype. An investigation was performed to determine the causes of discrepancies between the FE model and experimental results. Using information gained from this investigation, new composite beam designs were generated that compare the cost per weight-savings of different materials. Combining all of this information gives a better understanding of the feasibility of lightweight composite structural beams.

2 Analysis Methods

This section reviews the analysis methods used to design and analyze the composite beams. This includes the mechanics of thin-walled laminated beams (MTLB), FEA of composite beams, and a validation between the two.

2.1 Mechanics of Thin-Walled Laminated Beams

This section reviews the mechanics of thin-walled laminated beams as described in *Introduction to Composite Materials Design* by Ever J. Barbero [1]. It begins with single ply mechanics, moves to multiply ply mechanics, then expands to open-section beam mechanics.

2.1.1 Single Ply Mechanics

Two coordinate systems are defined in this section. Axes 1, 2, and 3 represent the material Cartesian coordinate system. The 1-axis is typically aligned with the fiber direction of the composite. The 2-axis is perpendicular to the 1-axis and lies in the plane of the composite shell. The 3-axis is perpendicular to the 1- and 2-axes and the composite shell. Figure 3 shows the material coordinate system axes with reference to a unidirectional ply.

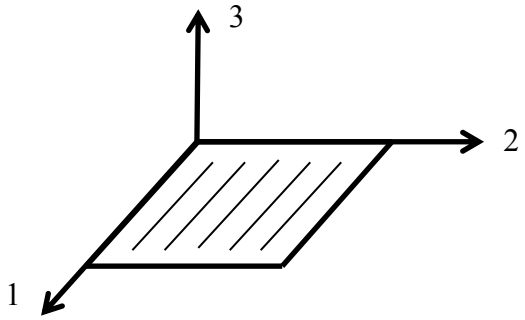

Figure 3 Material coordinate system axes 1, 2, and 3

When creating a laminate, another coordinate system must be defined. Axes x, s, and r represent the laminate Cartesian coordinate system. The r-axis is shared with the 3-axis of the material, and is the stacking direction when generating a laminate. A rotation of angle θ can be applied about the r-axis when creating plies of different orientation. The laminate coordinate system is shown in Figure 4. The r- and 3-axes point out of the page.

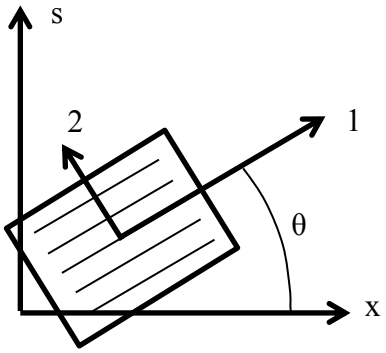

Figure 4 Laminate coordinate system relative to material coordinate system

The composite mechanics equations can be derived by first looking at the strain of a point in a composite material. In a general one dimensional case, strain of a point displaced a distance u is defined as

$$\epsilon_x = \lim_{\Delta L \to 0} \frac{\Delta L}{L} = \frac{du}{dx}$$

Expanding to the three dimensions of the laminate coordinate system, six components of strain are defined as partial derivatives of a point's displacement vector $\vec{u} = (u, v, w)$:

$$\epsilon_{xx} = \frac{\partial u}{\partial x}$$

$$\epsilon_{ss} = \frac{\partial v}{\partial s}$$

$$\epsilon_{rr} = \frac{\partial w}{\partial r}$$

$$\gamma_{xs} = \frac{\partial u}{\partial s} + \frac{\partial v}{\partial x}$$

$$\gamma_{xr} = \frac{\partial u}{\partial r} + \frac{\partial w}{\partial x}$$

$$\gamma_{sr} = \frac{\partial v}{\partial r} + \frac{\partial w}{\partial s}$$

The six components make up the strain tensor:

$$[\epsilon] = \begin{bmatrix} \epsilon_x & \frac{\gamma_{xs}}{2} & \frac{\gamma_{xr}}{2} \\ \frac{\gamma_{xs}}{2} & \epsilon_s & \frac{\gamma_{sr}}{2} \\ \frac{\gamma_{xr}}{2} & \frac{\gamma_{sr}}{2} & \epsilon_r \end{bmatrix}$$

Since the behavior of the laminate depends on the behavior of its plies, it is useful to write the strain tensor in terms of the material coordinate system:

$$[\epsilon] = \begin{bmatrix} \epsilon_{11} & \frac{\gamma_{12}}{2} & \frac{\gamma_{13}}{2} \\ \frac{\gamma_{12}}{2} & \epsilon_{22} & \frac{\gamma_{23}}{2} \\ \frac{\gamma_{13}}{2} & \frac{\gamma_{23}}{2} & \epsilon_{33} \end{bmatrix}$$

Since FRPs usually have small thickness relative to their width and length, they can be approximated as thin shells, which implies a through-the-thickness stress of zero ($\sigma_3 = 0$). The stress-strain equations can now be much more easily calculated for the plane stress state. A tensile stress, σ_1, applied along the 1-axis produces the following strain when all other stresses are set to zero. Note that all repeated subscript characters are reduced to a single character:

$$\epsilon_1 = \frac{\sigma_1}{E_1}$$

Applying a stress σ_2 along the 2-axis, with all other stresses set to zero, gives the following strain in the 1-direction using the definitions of Poisson's ratio:

$$\epsilon_1 = -\upsilon_{21}\epsilon_2 = -\upsilon_{21}\frac{\sigma_2}{E_2}$$

Summing the strain in the 1-direction gives

$$\epsilon_1 = \frac{1}{E_1}\sigma_1 - \frac{\upsilon_{21}}{E_2}\sigma_2$$

Similarly, if repeated transversely,

$$\epsilon_2 = -\frac{\upsilon_{12}}{E_1}\sigma_1 + \frac{1}{E_2}\sigma_2$$

The shear version of Hooke's law gives the following shear strains for a given shear stress:

$$\gamma_{12} = \frac{\sigma_{12}}{G_{12}}$$

$$\gamma_{23} = \frac{\sigma_{23}}{G_{23}}$$

$$\gamma_{13} = \frac{\sigma_{13}}{G_{13}} = \frac{\sigma_{13}}{G_{12}}$$

Since unidirectional laminae are transversely orthotropic, G_{13} is equivalent to G_{12}. Figure 5 demonstrates this with an end view of a unidirectional lamina. The 1-direction points out of the page.

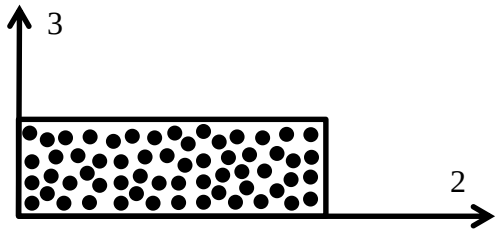

Figure 5 End view of unidirectional lamina

Putting the strain equations in matrix form gives

$$\begin{Bmatrix} \epsilon_1 \\ \epsilon_2 \\ \gamma_{12} \end{Bmatrix} = \begin{bmatrix} \frac{1}{E_1} & -\frac{v_{21}}{E_2} & 0 \\ -\frac{v_{12}}{E_1} & \frac{1}{E_2} & 0 \\ 0 & 0 & \frac{1}{G_{12}} \end{bmatrix} \begin{Bmatrix} \sigma_1 \\ \sigma_2 \\ \sigma_{12} \end{Bmatrix}$$

$$\begin{Bmatrix} \gamma_{23} \\ \gamma_{13} \end{Bmatrix} = \begin{bmatrix} \frac{1}{G_{23}} & 0 \\ 0 & \frac{1}{G_{13}} \end{bmatrix} \begin{Bmatrix} \sigma_{23} \\ \sigma_{13} \end{Bmatrix}$$

Since the compliance matrix must be symmetric, this implies that $v_{21}/E_2 = v_{12}/E_1$. Shear stresses σ_{23} and σ_{13} can be ignored for a thin plate. Shortening the notation gives

$$\{\epsilon\} = [S]\{\sigma\}$$

$$\{\gamma\} = [S^*]\{\tau\}$$

Inverting $[S]$ and $[S^*]$ gives

$$\{\sigma\} = [Q]\{\epsilon\}$$

$$\{\epsilon\} = [Q^*]\{\sigma\}$$

$[Q]$ is the reduced stiffness matrix and $[Q^*]$ is the intralaminar stiffness matrix:

$$[Q] = \begin{bmatrix} \frac{E_1}{\Delta} & \frac{v_{12}E_2}{\Delta} & 0 \\ \frac{v_{12}E_2}{\Delta} & \frac{E_2}{\Delta} & 0 \\ 0 & 0 & G_{12} \end{bmatrix}$$

$$[Q^*] = \begin{bmatrix} G_{23} & 0 \\ 0 & G_{13} \end{bmatrix}$$

where

$$\Delta = 1 - v_{12}v_{21} = 1 - v_{12}^2\frac{E_2}{E_1}$$

2.1.2 Multiple Ply Mechanics

As described earlier, it is useful to construct a laminate with multiple plies at varying orientations. In order to have the reduced stiffness matrix of a ply in the laminate coordinate system, a coordinate transformation must take place. A transformation matrix is generated by looking at a displacement vector with respect to both coordinate systems and using the chain rule to compute the strains with respect to the original coordinate system. This results in the following transformation matrices:

$$[T] = \begin{bmatrix} \cos^2\theta & \sin^2\theta & 2\cos\theta\sin\theta \\ \sin^2\theta & \cos^2\theta & -2\cos\theta\sin\theta \\ -\cos\theta\sin\theta & \cos\theta\sin\theta & \cos^2\theta - \sin^2\theta \end{bmatrix}$$

$$[T^*] = \begin{bmatrix} \cos\theta & \sin\theta \\ -\sin\theta & \cos\theta \end{bmatrix}$$

The transformed reduced stiffness matrix is now

$$[\bar{Q}] = [T]^{-1}[Q][T]^{-T}$$

where $[T]^{-T}$ is the transpose of the inverse of $[T]$. The transformed reduced stiffness matrix components can be written as

$$[\bar{Q}] = \begin{bmatrix} \bar{Q}_{11} & \bar{Q}_{12} & \bar{Q}_{16} \\ \bar{Q}_{12} & \bar{Q}_{22} & \bar{Q}_{26} \\ \bar{Q}_{16} & \bar{Q}_{26} & \bar{Q}_{33} \end{bmatrix}$$

When combining multiple laminae into a laminate, it is necessary to calculate the laminate stiffness matrix. The laminate stiffness matrix is made up of three sub-matrices: the $[A]$, $[B]$, and $[D]$ matrices. For convenience, the laminate stiffness matrix relates forces and moments to strains and curvatures, as opposed to relating stress to strain. The $[A]$ matrix, known as the in-plane stiffness matrix, relates in-plane per-unit-width forces (N_x, N_s, N_{xs}) to in-plane strains (ϵ_x^0, ϵ_s^0, ϵ_{xs}^0). The $[D]$ matrix, known as the bending stiffness matrix, relates per-unit-width bending moments (M_x, M_s, M_{xs}) to curvatures (κ_x, κ_s, κ_{xs}). The $[B]$ matrix, known as the bending-extension coupling matrix, relates bending moments to in-plane strains and in-plane forces to curvatures. This matrix is zero for isotropic materials or for symmetric layups. The orientation of the bending moments and forces are depicted in Figure 6.

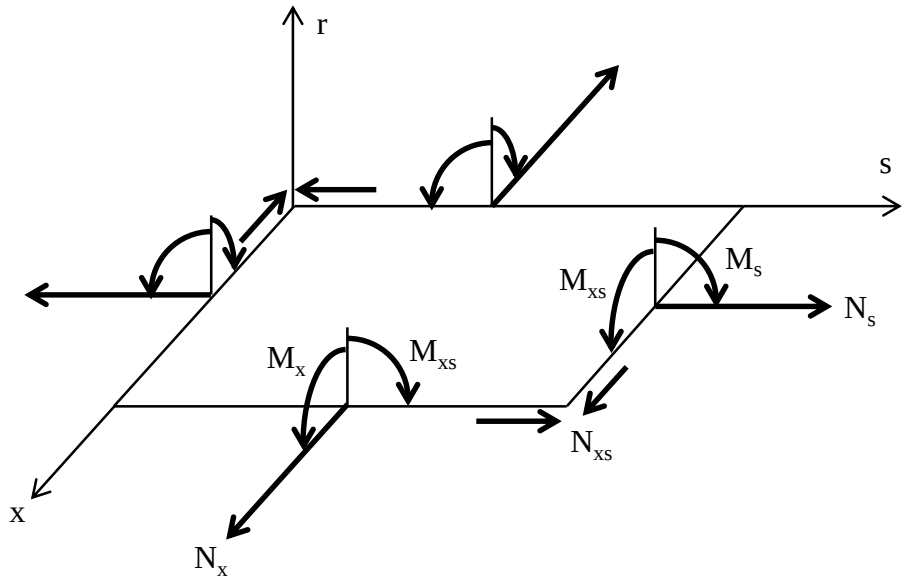

Figure 6 Force and moment diagram on a laminate

The laminate stiffness equations are

$$\begin{Bmatrix} N_x \\ N_s \\ N_{xs} \\ M_x \\ M_s \\ M_{xs} \end{Bmatrix} = \begin{bmatrix} A_{11} & A_{12} & A_{16} & B_{11} & B_{12} & B_{16} \\ A_{12} & A_{22} & A_{26} & B_{12} & B_{22} & B_{26} \\ A_{16} & A_{26} & A_{66} & B_{16} & B_{26} & B_{66} \\ B_{11} & B_{12} & B_{16} & D_{11} & D_{12} & D_{16} \\ B_{12} & B_{22} & B_{26} & D_{12} & D_{22} & D_{26} \\ B_{16} & B_{26} & B_{66} & D_{16} & D_{26} & D_{66} \end{bmatrix} \begin{Bmatrix} \epsilon_x^0 \\ \epsilon_x^0 \\ \gamma_{xs}^0 \\ \kappa_x \\ \kappa_s \\ \kappa_{xs} \end{Bmatrix}$$

where

$$A_{ij} = \sum_{k=1}^{N} \left(\bar{Q}_{ij}\right)_k t_k; i,j = 1,2,6$$

$$B_{ij} = \sum_{k=1}^{N} \left(\bar{Q}_{ij}\right)_k t_k \bar{r}_k; i,j = 1,2,6$$

$$D_{ij} = \sum_{k=1}^{N} \left(\bar{Q}_{ij}\right)_k \left(t_k \bar{r}_k^2 + \frac{t_k^2}{12}\right); i,j = 1,2,6$$

t_k represents the thickness of k-th lamina, and $\bar{r}_k$ is the r-coordinate of the mid-plane of the k-th lamina out of N total laminae. These are depicted in Figure 7.

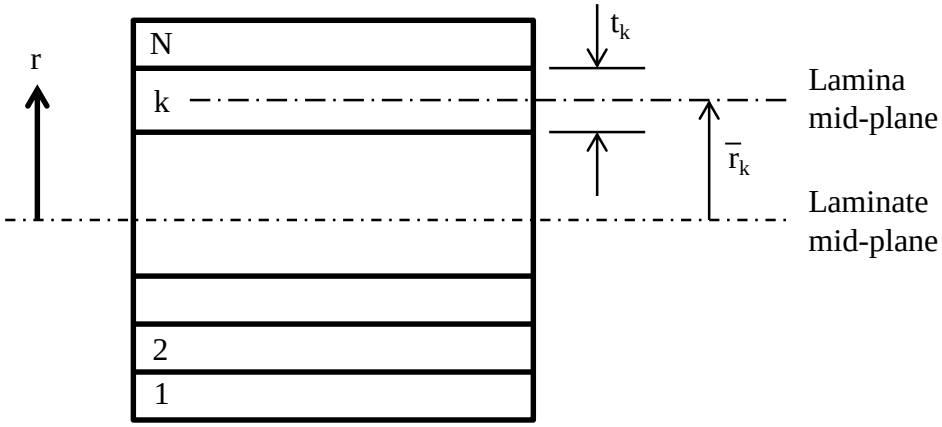

Figure 7 Laminate geometry composed of N laminae

Inverting the laminate stiffness matrix gives the laminate compliance matrix and the following equations:

$$\begin{Bmatrix} \epsilon_x^0 \\ \epsilon_s^0 \\ \gamma_{xs}^0 \\ \kappa_x \\ \kappa_s \\ \kappa_{xs} \end{Bmatrix} = \begin{bmatrix} \alpha_{11} & \alpha_{12} & \alpha_{16} & \beta_{11} & \beta_{12} & \beta_{16} \\ \alpha_{12} & \alpha_{22} & \alpha_{26} & \beta_{12} & \beta_{22} & \beta_{26} \\ \alpha_{16} & \alpha_{26} & \alpha_{66} & \beta_{16} & \beta_{26} & \beta_{66} \\ \beta_{11} & \beta_{12} & \beta_{16} & \delta_{11} & \delta_{12} & \delta_{16} \\ \beta_{12} & \beta_{22} & \beta_{26} & \delta_{12} & \delta_{22} & \delta_{26} \\ \beta_{16} & \beta_{26} & \beta_{66} & \delta_{16} & \delta_{26} & \delta_{66} \end{bmatrix} \begin{Bmatrix} N_x \\ N_s \\ N_{xs} \\ M_x \\ M_s \\ M_{xs} \end{Bmatrix}$$

2.1.3 Open Section Beam Mechanics

Multiple laminates, or segments, can be combined to give the overall bending and torsional stiffnesses of open section beams, such as a c-channel beam. This section reviews the individual segment definitions and how they are combined for bending, torsional, and shear stiffness.

2.1.3.1 Segment Property Definitions

The summation of multiple segments into an overall beam profile requires the definition of several new terms. A global beam coordinate system (X,Y,Z) with the X-axis along the length of the beam, the Y-axis running horizontally, and the Z-axis running vertically is defined. This coordinate system is the same as the one shown in Figure 1. The x-axis of the (x,s,r) laminate coordinate system lines up with the X-axis of the global coordinate system. The s- and r-axes of the ith segment are offset from the Y- and Z-axes by the rotation angle φ^i. The width of a segment is denoted as b^i and the segment thickness is t^i. These terms, along with new ones that are explained in later sections, are shown in Figure 8.

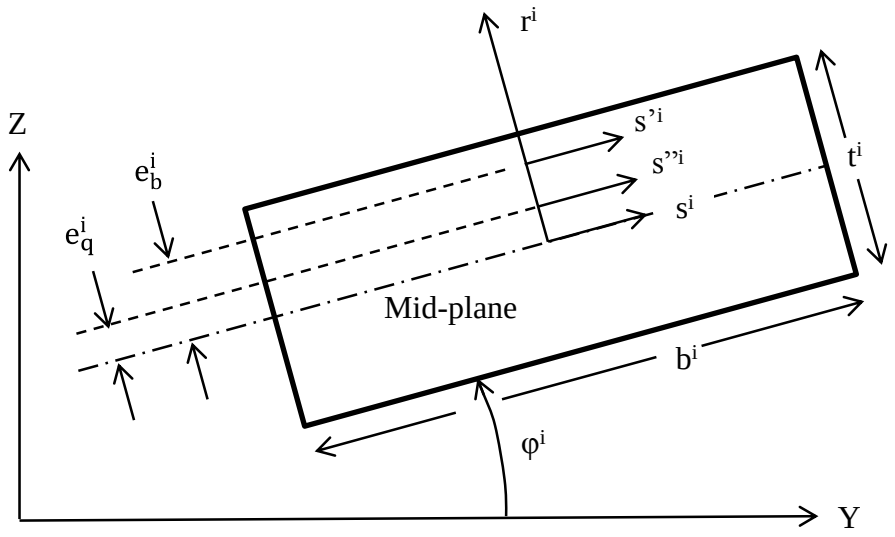

Figure 8 Diagram showing segment terms

Several segments can be linked together to form the overall beam profile. Figure 9 shows the numbering system for segments (circled) and nodes for a four segment cross-section in the global coordinate system.

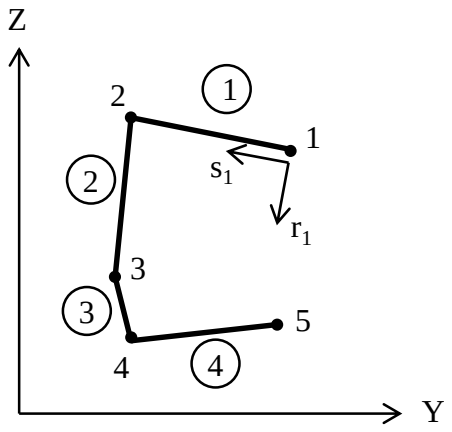

Figure 9 Segment (circled) and node numbering system for a four segment cross-section. The X-axis and x-axis point out of the page.

Returning to the compliance equations for the ith segment, they are now

$$\begin{Bmatrix} \epsilon_x^i \\ \epsilon_s^i \\ \gamma_{xs}^i \\ \kappa_x^i \\ \kappa_s^i \\ \kappa_{xs}^i \end{Bmatrix} = \begin{bmatrix} \alpha_{11} & \alpha_{12} & 0 & \beta_{11} & \beta_{12} & 0 \\ \alpha_{12} & \alpha_{22} & \alpha_{26} & \beta_{12} & \beta_{22} & \beta_{26} \\ 0 & \alpha_{26} & \alpha_{66} & 0 & \beta_{26} & \beta_{66} \\ \beta_{11} & \beta_{12} & 0 & \delta_{11} & \delta_{12} & 0 \\ \beta_{12} & \beta_{22} & \beta_{26} & \delta_{12} & \delta_{22} & \delta_{26} \\ 0 & \beta_{26} & \beta_{66} & 0 & \delta_{26} & \delta_{66} \end{bmatrix} \begin{Bmatrix} N_x^i \\ N_s^i = 0 \\ N_{xs}^i \\ M_x^i \\ M_s^i = 0 \\ M_{xs}^i \end{Bmatrix}$$

where transverse forces and moments ($N_s^i \; and \; M_s^i$) are assumed to be negligible compared to the axial forces and moments. The terms α_{16}, β_{16}, and δ_{16} are also negligible for balanced symmetric laminates, which uncouples the normal and shearing effects. If laminates are not symmetric and balanced, this method still provides approximate results. The strain, ϵ_s^i, and curvature, κ_s^i, can also be ignored as they are no longer needed. The compliance equations are now reduced and rearranged to give:

$$\begin{Bmatrix} \epsilon_x^i \\ \kappa_x^i \\ \gamma_{xs}^i \\ \kappa_{xs}^i \end{Bmatrix} = \begin{bmatrix} \alpha_{11} & \beta_{11} & 0 & 0 \\ \beta_{11} & \delta_{11} & 0 & 0 \\ 0 & 0 & \alpha_{66} & \beta_{66} \\ 0 & 0 & \beta_{66} & \delta_{66} \end{bmatrix} \begin{Bmatrix} N_x^i \\ M_x^i \\ N_{xs}^i \\ M_{xs}^i \end{Bmatrix}$$

Inverting these equations gives the following reduced stiffness equations:

$$\begin{Bmatrix} N_x^i \\ M_x^i \\ N_{xs}^i \\ M_{xs}^i \end{Bmatrix} = \begin{bmatrix} A_i & B_i & 0 & 0 \\ B_i & D_i & 0 & 0 \\ 0 & 0 & F_i & C_i \\ 0 & 0 & C_i & H_i \end{bmatrix} \begin{Bmatrix} \epsilon_x^i \\ \kappa_x^i \\ \gamma_{xs}^i \\ \kappa_{xs}^i \end{Bmatrix}$$

All properties needed to solve for overall beam stiffness are based on the segment properties A_i, B_i, C_i, D_i, F_i, and H_i. A_i is the axial stiffness per unit width; B_i couples bending curvature, κ_x^i, and force N_x^i; C_i couples twisting curvature, κ_{xs}^i, and shear, N_{xs}^i; D_i is the bending stiffness when subjected to M_x^i; F_i is the in-plane shear stiffness when subjected to N_{xs}^i; and H_i is the torsional stiffness under moment, M_{xs}^i.

2.1.3.2 Bending Stiffness

Two terms are introduced to help solve for the bending stiffness of a beam. The term e_b^i is now introduced which represents the distance from the mid-plane along the r-direction to the neutral axis of bending. This term is depicted in Figure 8. Any force N_x^i applied at this point will produce no bending curvature κ_x^i. It is solved for by assuming all strains and curvatures are zero except ϵ_x^i. This causes the stiffness equations to reduce to

$$N_x^i = A_i \epsilon_x^i$$

$$M_x^i = B_i \epsilon_x^i$$

Solving for ϵ_x^i and substituting gives

$$M_x^i = e_b^i N_x^i$$

where

$$e_b^i = \frac{B_i}{A_i}$$

A new coordinate system (x,s',r) is created at the neutral axis of bending that is a distance e_b^i away from the laminate mid-plane coordinate system (x,s,r) as shown in Figure 8.

The term e_b^i is used to solve for $\bar{D}_\iota$, which also assists in calculating bending stiffness. $\bar{D}_\iota$ is the segment bending stiffness D_i but with respect to the s'-axis. It is calculated by setting $N_x^i = 0$ and looking at the first two reduced stiffness equations:

$$0 = A_i \epsilon_x^i + B_i \kappa_x^i$$

$$M_x^i = B_i \epsilon_x^i + D_i \kappa_x^i$$

Solving for ϵ_x^i and substituting gives

$$M_x^i = \left(D_i - \frac{(B_i)^2}{A_i} \right) \kappa_x^i$$

The term in the parenthesis can be replaced by $\bar{D}_\iota$, where

$$\bar{D}_\iota = D_i - \left(e_b^i\right)^2 A_i$$

The bending stiffness of beams made from isotropic materials is the elastic modulus, E, times the second moments of area, I_{YY} and I_{ZZ}. For a laminated beam the bending stiffnesses for each segment are

$$(EI_{s'}^i) = \bar{D}_\iota b_i$$

$$(EI_{r'}^i) = A_i \, b_i^3 / 12$$

These bending stiffnesses are in terms of the neutral axis of bending for each segment (x,s',r'). Transforming them into the global coordinate system (X,Y,Z) by the segment angle φ_i gives

$$(EI_Y^i) = (EI_{s'}^i)\cos^2\varphi_i + (EI_{r'}^i)\sin^2\varphi_i$$

$$(EI_Z^i) = (EI_{s'}^i)\sin^2\varphi_i + (EI_{r'}^i)\cos^2\varphi_i$$

where (EI_Y^i) is the vertical bending stiffness and (EI_Z^i) is the lateral bending stiffness for each section. The bending stiffness of each segment can be summed using the parallel axis theorem to get the global vertical bending stiffness (EI_{YG}) and lateral bending stiffnesses (EI_{ZG}) of the beam, denoted with an additional subscript G:

$$(EI_{YG}) = \sum_{i=1}^{n}\left[(EI_Y^i) + A_i b_i\left(z_i + e_b^i\cos\varphi_i\right)^2\right]$$

$$(EI_{ZG}) = \sum_{i=1}^{n}\left[(EI_Z^i) + A_i b_i\left(y_i + e_b^i\sin\varphi_i\right)^2\right]$$

2.1.3.3 Torsional Stiffness

Two terms are introduced to assist in solving for torsional stiffness. The term e_q^i represents the distance from the mid-plane along the r-axis to the neutral axis of torsion. This term is depicted in Figure 8. It is solved for by setting all strains and curvatures equal to zero except the shear strain γ_{xs}^i. The last two reduced stiffness equations become

$$N_{xs}^i = F_i\gamma_{xs}^i$$

$$M_{xs}^i = C_i\gamma_{xs}^i$$

Solving for γ_{xs}^{i} and substituting gives

$$M_{xs}^{i} = e_{q}^{i} N_{xs}^{i}$$

where

$$e_{q}^{i} = \frac{C_i}{F_i}$$

A new coordinate system (x,s",r) is created at the neutral axis of torsion that is a distance e_{q}^{i} away from the laminate mid-plane coordinate system (x,s,r), as shown in Figure 8.

The term e_{q}^{i} is used to solve for $\overline{H_{\iota}}$, which also assists in calculating torsional stiffness. $\overline{H_{\iota}}$ is the segment torsional stiffness H_i but with respect to the s"-axis. It is calculated by setting $N_{xs}^{i} = 0$ and looking at the last two reduced stiffness equations:

$$0 = F_i \gamma_{xs}^{i} + C_i \kappa_{xs}^{i}$$

$$M_{xs}^{i} = C_i \gamma_{xs}^{i} + H_i \kappa_{xs}^{i}$$

Solving for γ_{xs}^{i} and substituting gives

$$M_{xs}^{i} = \left(H_i - \frac{(C_i)^2}{F_i} \right) \kappa_{xs}^{i}$$

The term in the parenthesis can be replaced by $\overline{H_{\iota}}$, where

$$\overline{H_{\iota}} = H_i - \left(e_{q}^{i}\right)^2 F_i$$

The torsional stiffness of an isotropic beam is the shear modulus, G, times the polar moment of inertia, J. For a laminated beam, the torsional stiffness of each segment is

$$\left(GJ_{R}^{i}\right) = 4\overline{H_{\iota}} b_i$$

The factor of four is a result of the integration performed when balancing energy between the work done by external torque and the strain energy. The beam's global torsional stiffness is the sum each segments' torsional stiffness:

$$(GJ_R) = 4\sum_{i=1}^{n}[\bar{H}_i b_i]$$

2.1.3.4 Shear Stiffness

It is necessary to incorporate shear deformation into composite beam models. Since metals tend to have higher shear modulus than composites, the shear deformation is usually negligible compared to bending deformation, especially for long metal beams. However, this is not the case for composite beams where shear deformation contributes a significant portion to overall beam deformation [1].

The shear stiffness (GA) of beams can be approximated as the effective shear modulus of the web times the area of the web [1] [12]. The effective shear modulus of a segment is the shear stiffness per unit width, F_i, of the segment divided by its thickness:

$$G_{xs}^{i} = \frac{F_i}{t_i}$$

Multiplying the effective shear modulus by the area gives

$$G_{xs}^{i} A_i = \frac{F_i}{t_i} b_i t_i = F_i b_i$$

Note that in the above equation, A_i represents the cross-sectional area of the segment, and not the axial stiffness per unit width. The validity of this approximation is covered in the following section.

2.2 MTLB and FEA Agreement

In order to know that the assumptions and approximations used in the MTLB theory are accurate, MTLB must be validated against FEA and other analytical methods. This section reviews the validation of a MATLAB program based on MTLB against an FE model for a composite beam, and against an FE model and analytical model for a steel beam. The MTLB MATLAB code can be seen in APPENDIX A.

2.2.1 Composite Beam Validation

A composite c-channel beam was modeled using MTLB and FEA. The beam had a constant ply-layup of $[0/45/-45/90]_S$ along the entire profile. Each ply was assigned the SM unidirectional CFRP properties with a W_f of 72.4%, as shown in Table 2. Each ply was 0.05 in thick, for a total laminate thickness of 0.40 in. The beam was 10 in high, 3.5 in wide, and 100 in long. Vertical bending stiffness is reported as an "effective" bending stiffness, as it combines both bending and shear deformation. Since shear deformation depends on of the length of the beam, and bending deformation depends on the cube of the length of the beam, the effective stiffness is only valid for a length of 100 in. The length of the beam in the torsion model is 1500 in. The MTLB and FEA results are shown in Table 3.

Table 3 MTLB and FEA validation for composite c-channel beam

Composite Beam Model Type	**Effective $EI_{vertical}$ ($lbs*in^2$)**	**Effective $EI_{vertical}$ Error**	**$EI_{lateral}$ ($lbs*in^2$)**	**$EI_{lateral}$ Error**	**$GJ_{torsional}$ ($lbs*in^2$)**	**$GJ_{torsional}$ Error**
MTLB	6.78E+08	-	5.40E+07	-	7.94E+05	-
FEA	6.79E+08	0.08%	5.37E+07	-0.52%	7.93E+05	-0.17%

MTLB and FEA agreed very well in both bending and torsion, with both errors under 1%, although it took several FE models of increasing beam length before torsional agreement was reached. The good agreement in vertical bending stiffness shows that the shear stiffness approximation used in the MTLB model is appropriate, since it matches the FE model which considers shear effects. It took several models of increasing length until torsion was validated. Open section beams have lower torsional stiffness than closed section beams since the material is free to deform out of the plane of torsion. Because normal fixed constraints of an FE model constrain this deformation, the boundary effects are very noticeable for shorter beam lengths. As beam length increases, the torsional stiffness of the FE model approaches that of the MTLB model, as shown in Table 4 and Figure 10. The results show that the approximations and assumptions made using MTLB are valid for composite beam modeling.

Table 4 FEA torsional stiffness error vs. beam length for composite beam

MTLB $GJ_{torsional}$ ($lbs*in^2$)	**FEA $GJ_{torsional}$ ($lbs*in^2$)**	**FEA $GJ_{torsional}$ Error**	**Beam Length (in)**
7.94E+05	1.86E+06	134%	100
7.94E+05	8.72E+05	9.76%	500
7.94E+05	8.11E+05	2.14%	1000
7.94E+05	7.93E+05	-0.17%	1500

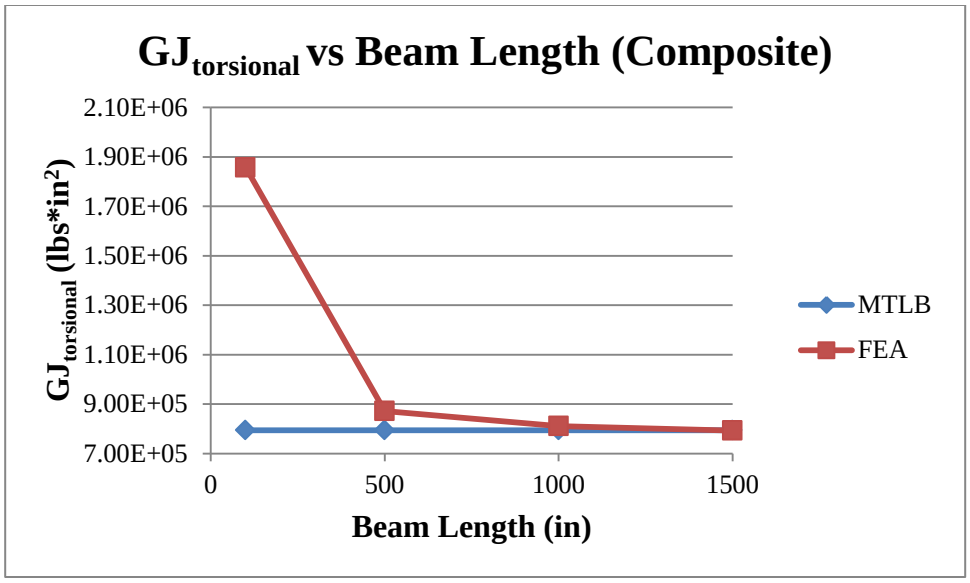

Figure 10 Torsional stiffness vs. beam length for FE and MTLB composite beam models

2.2.2 Steel Beam Validation

A steel c-channel beam was also modeled using FEA, MTLB, and beam formulas. This was done in order to validate the FE and MTLB models against the basic beam deflection formulas. Again, the effective vertical bending stiffness combined the deformations of both bending and shear deformation. The beam formulas used are deflection due to bending,

$$\delta = \frac{PL^3}{EI}$$

deflection due to shear,

$$\delta = \frac{PL}{GA}$$

and angular deflection due to torsion,

$$\theta = \frac{TL}{GJ}$$

where

$$J = \frac{pt^3}{3}$$

P is the applied load, L is the length of the beam, E is the elastic modulus, p is the perimeter length of the mid-plane of the beam profile, and t is the thickness of the profile. The second moment of area, I, was calculated automatically using section analysis in SolidWorks. Like the MTLB model, shear stiffness was approximated as the shear modulus, G, times the area of the web, A. The same geometry as the composite beam was used for the steel beam, except all composite material properties were replaced with nominal steel properties. The results of all three models are shown in Table 5.

Table 5 MTLB, FEA, and beam formula validation for steel c-channel beam

Steel Beam Model Type	**Effective $EI_{vertical}$ (lbs*in^2)**	**Effective $EI_{vertical}$ Error**	**$EI_{lateral}$ (lbs*in^2)**	**$EI_{lateral}$ Error**	**$GJ_{torsional}$ (lbs*in^2)**	**$GJ_{torsional}$ Error**
MTLB	2.40E+09	-	1.90E+08	-	3.74E+06	-
FEA	2.41E+09	0.33%	1.90E+08	0.03%	3.80E+06	1.62%
Beam Formulas	2.41E+09	0.20%	1.91E+08	0.23%	3.74E+06	-0.001%

Like the composite beam, vertical and lateral bending stiffness agreed very well, with all errors under 0.25%, but it took several FE models until torsion agreed. The same increasing beam length models were used until error between the FE model and analytical model was negligible. These results are shown in Table 6 and Figure 11.

The results show that the assumptions and approximations used in MTLB are valid for both composite and steel beam modeling.

Table 6 FEA torsional stiffness error vs. beam length for steel beam.

MTLB $GJ_{torsional}$ ($lbs*in^2$)	FEA $GJ_{torsional}$ ($lbs*in^2$)	FEA $GJ_{torsional}$ Error	Beam Length (in)
3.74E+06	7.73E+06	107%	100
3.74E+06	4.12E+06	10.1%	500
3.74E+06	3.87E+06	3.62%	1000
3.74E+06	3.80E+06	1.62%	1500

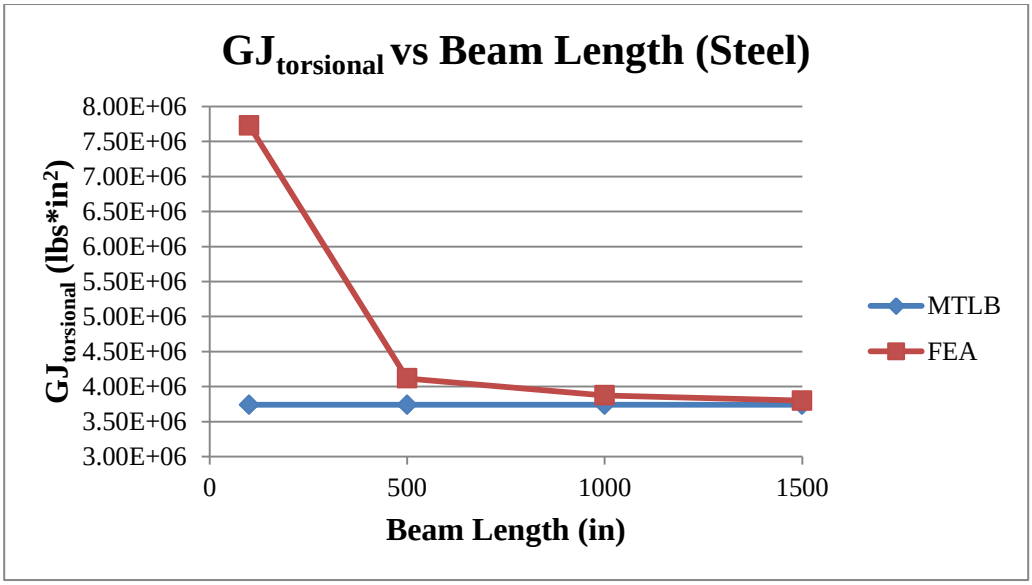

Figure 11 Torsional stiffness vs. beam length for FE and MTLB steel beam models

3 Prototype-A Manufacturing and Full Beam Testing

The prototype-A beam was manufactured and underwent physical testing. This section reviews the pultrusion process used to create the prototype, the full beam test setup, and the results from the full beam testing.

3.1 Pultrusion Process

A pultrusion process was used to manufacture the prototype-A CFRP beam. Pultrusion is a high volume, continuous manufacturing process for creating FRP parts of any length with a constant cross-section [13]. This is an ideal method for creating constant cross-section beams such as c-channel structural beams. The process begins with reels of fiber roving and fabrics. The fibers are drawn from the reels and pulled through preforming guides that begin to shape the profile of the beam. The fibers are then wetted as they are pulled through a resin bath and into the heated die. The heated die squeezes excess resin off, cures the remaining resin, and sets the final cross-sectional shape. After exiting the die, the cured beam passes through the pulling system and into the cutting station where it is cut to length. After the beam is cut, additional trimming and machining can be performed to drill holes and achieve the proper finish and geometry.

3.2 Prototype-A Full Beam Testing Setup

The prototype-A beam was tested in a cantilever configuration to measure vertical bending, lateral bending, and torsional stiffness response. The web of the rear of the beam was bolted to a base with a 1 in thick steel plate and ten 7/8 in bolts, as shown in Figure 12.

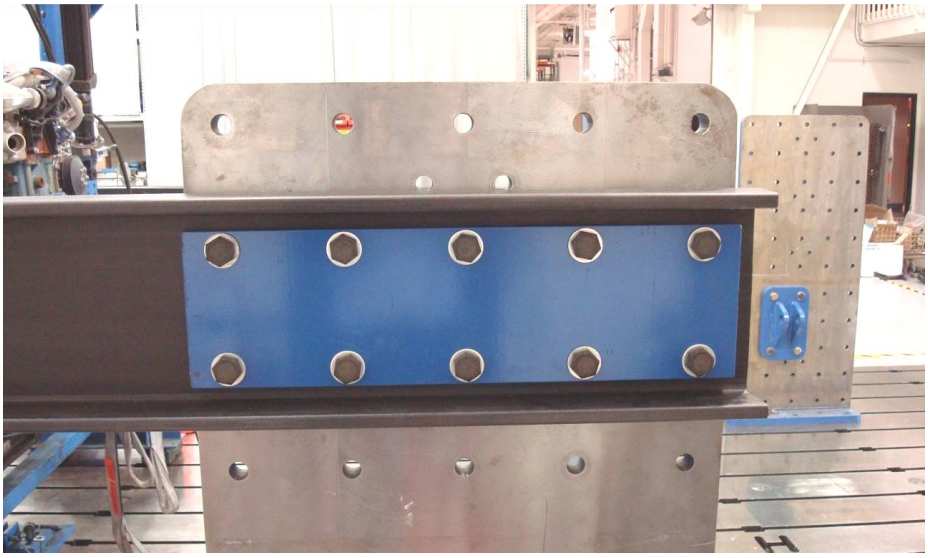

Figure 12 Rear of Prototype-A beam bolted to base

Two 1/2 in thick steel plates were bolted on either side of the web of the front of the beam. This allowed for the bending and torque loads to be properly applied to the beam. Vertical bending loads were applied by hanging weights from a bolt at the shear center from one of the steel plates. The loads were measured with a load cell, and the displacement was measured with a string potentiometer. The vertical loading configuration is shown in Figure 13.

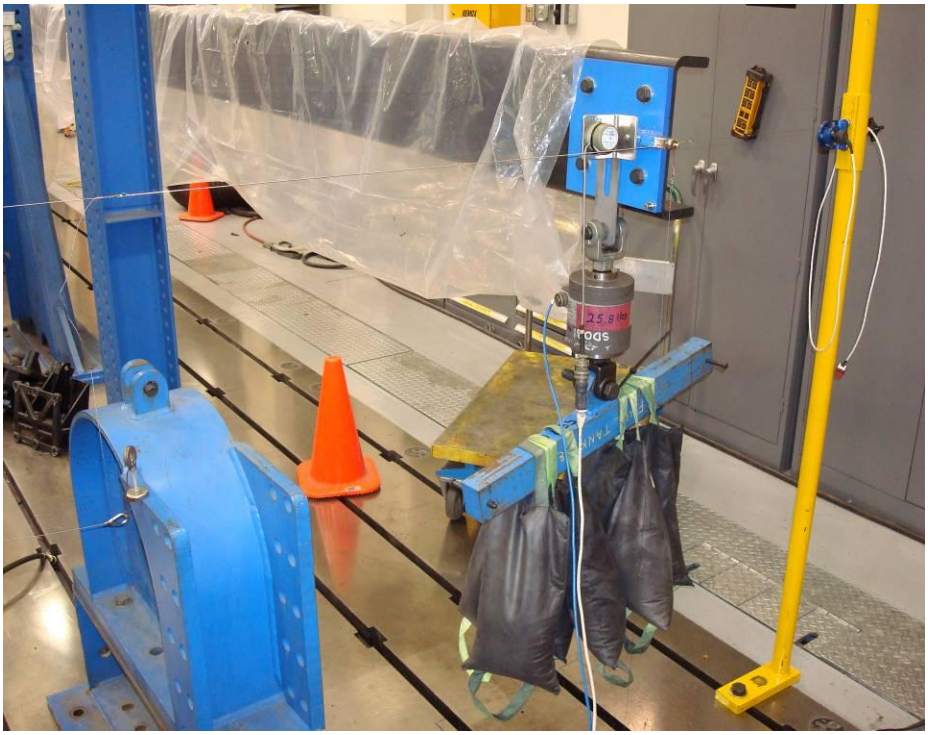

Figure 13 Vertical loads applied to prototype-A beam

Lateral bending loads were applied through a wire attached to the steel plates. Displacement was also measured using a string potentiometer. The wires are also shown in Figure 13, but may be difficult to see. Torque was applied to a 0.75 in square bar welded to one of the steel plates. Torque was measured using a torque transducer, and deflection angle was measured using an inclinometer. The torque loading configuration is shown in Figure 14.

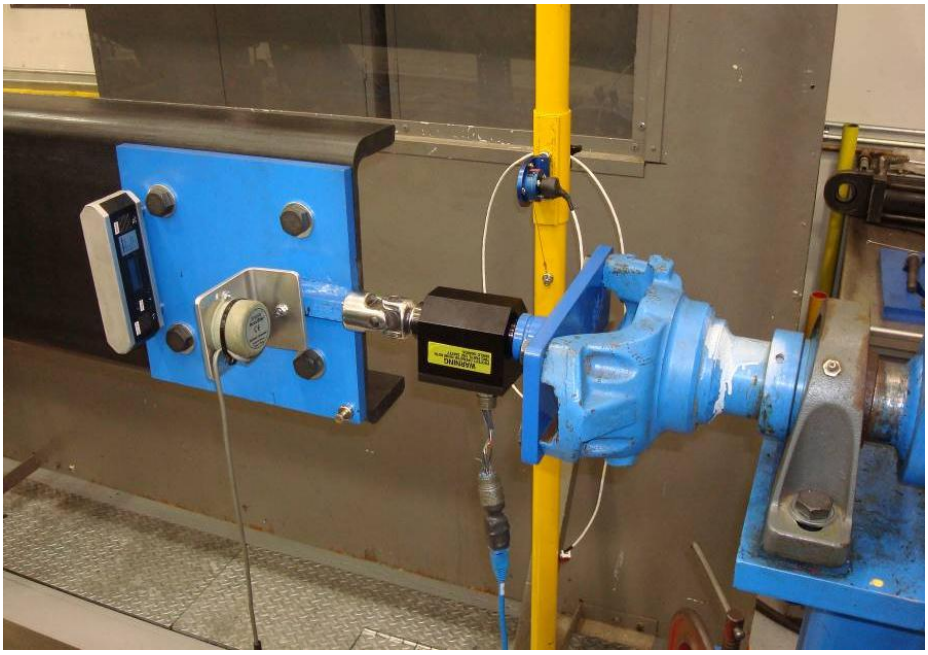

Figure 14 Torque loads applied to prototype-A beam

3.3 Prototype-A Full Beam Testing Results

Load and deflection data was recorded in order to measure the vertical bending, lateral bending, and torsional stiffness response. Loads and deflections were measured at many different load levels and plotted on a load versus deflection graph. The data was linear curve-fit, with the slope of the line representing the average stiffness, or spring rate, of each loading case. Ignoring the intercept of the line allows the natural deflection of the beam under its own weight to be ignored. The spring rates for each loading case are shown in Table 7. The reported lateral spring rate is an average of the spring rates in the positive and negative lateral direction.

Table 7 Prototype-A full beam testing results

Vertical Spring Rate (lb/in)	Lateral Spring Rate (lb/in)	Torsional Spring Rate (in*lb/°)
561	29.6	147

Due to the nature of the loading and boundary conditions, these spring rates cannot be directly compared against the original stiffness targets of the prototype-A beam. Instead, an FE model of the prototype-A beam that incorporates the loading and boundary conditions was necessary.

4 FE Modeling of Prototype-A Full Beam Testing

An FE model of the prototype-A beam was generated in order to compare to the full beam testing results reported in the previous section. This section reviews the FE modeling process of the prototype-A beam and the stiffness results from the model.

4.1 FE Modeling of Test Setup

The FE model of the prototype-A beam was generated to accurately represent the loading and boundary conditions of the physical testing. The clamping of the rear of the beam to the base was modeled with a fixed boundary condition the same size as the clamping plate. This clamped area is shown in red in Figure 15 and is analogous to Figure 12.

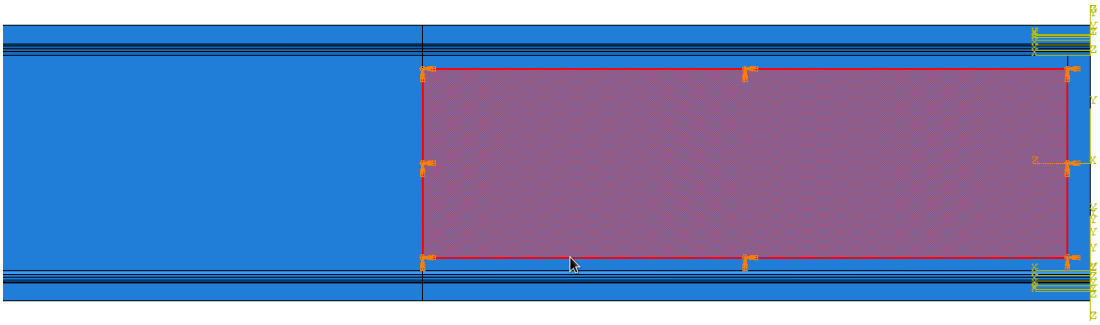

Figure 15 Clamped boundary condition for prototype-A FE model

The steel plates attached to the front of the beam were modeled as sections with steel properties that share nodes with the beam. The bolt that carried the vertical loads was modeled as a small section protruding from the outer steel plate. The 0.75 in steel bar which carried the torque and lateral loads was also connected to the outer steel plate. Point loads and torques were applied to these sections in the same location as the physical test. These loads are shown in Figure 16.

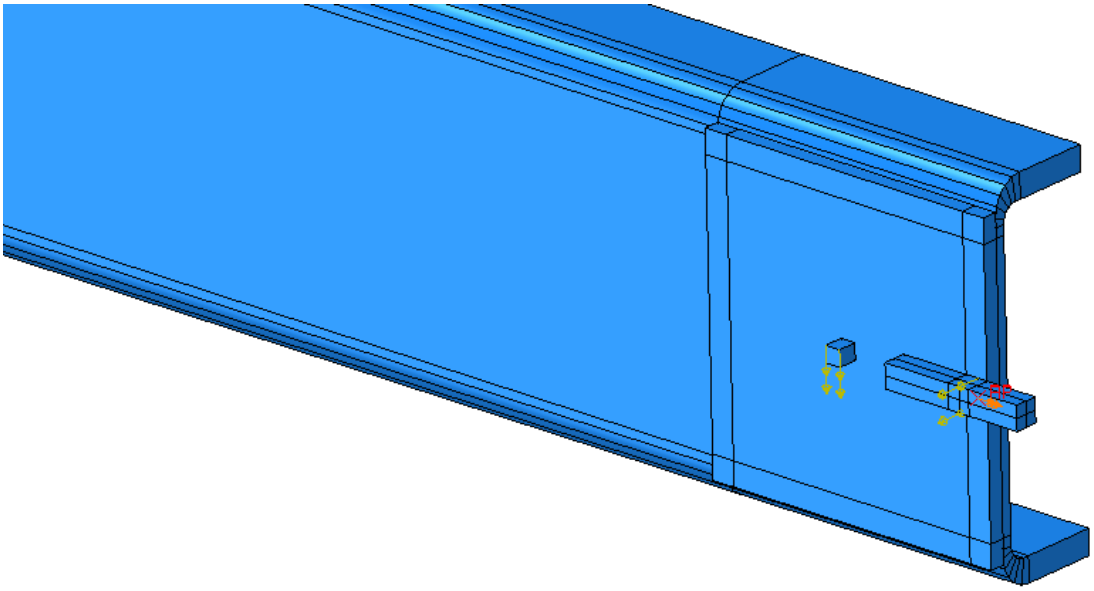

Figure 16 Loads applied to steel sections of prototype-A FE model

The sections were meshed with two different element types. The beam was meshed with continuum shell elements (Abaqus element number SC8R), which are appropriate due to the thin plate nature of the sections of beam. The steel plates at the front of the beam were meshed with 3D stress elements, without reduced integration (Abaqus element number C3D8). These were chosen in order to properly transfer all loads from the steel plates to the beam. The sections were meshed with a global element size of 0.55 in. This size proved to be small enough to reach mesh convergence for deflections. Each section contained one element through the thickness, with the exception of the steel sections attached to the steel plate. The radius of the beam contained six elements throughout the transition. This number was also shown to be refined enough to reach mesh convergence and remove any errors regarding skewed elements. The mesh is shown in Figure 17 with the beam shown in yellow and the steel sections shown in blue. The material properties and layup applied to the model are the same as those described in the prototype-A background section.

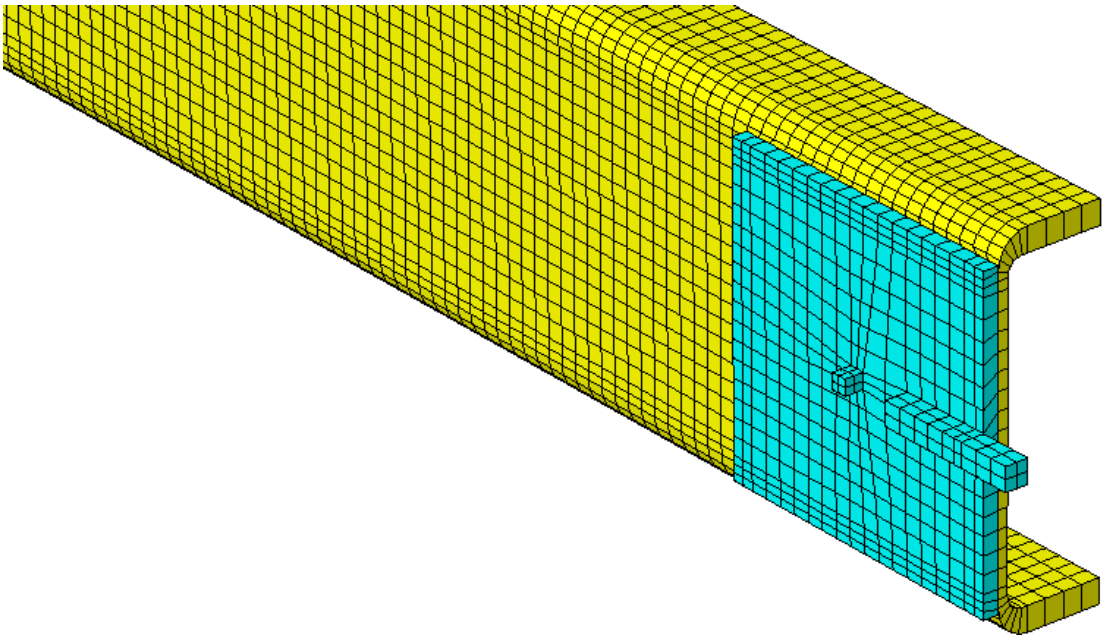

Figure 17 Meshed FE model of prototype-A beam (yellow) and steel sections (blue)

4.2 FE Model Results

The applied loads of the FE model were divided by the measured deflections to calculate the spring rates for vertical bending, lateral bending, and torsion, in order to compare to the physical testing. The results from the FE modeling are shown in Table 8 along with the physical results and the error between the two.

Table 8 Prototype-A beam FE model results compared to physical results

Prototype-A Beam Type	Vertical Spring Rate (lb/in)	Vertical Spring Rate Error	Lateral Spring Rate (lb/in)	Lateral Spring Rate Error	Torsional Spring Rate (in*lb/°)	Torsional Spring Rate Error
Physical Testing	561	-	29.6	-	147	-
Original FE Model	830	48.0%	43.3	46.3%	211	44.0%

Table 8 above shows considerable error between FE model results and the physical testing. This error prompted an investigation into the sources of error that is covered in the following section.

5 Adjustments to Prototype-A Beam FE Model

The considerable discrepancies between FE model results and physical testing shown in Table 8 prompted adjustments to the FE model. An investigation was performed to determine the sources of error in the FE model. The suspected sources of error in the FE model include inaccurate material properties, beam geometry, and boundary conditions. This section reviews the adjustments made to the FE model and their impact on the error compared to physical testing. These adjustments include changes to geometry, changes to material properties based on fiber content, changes to material properties based on tensile specimen testing, and a method of determining if boundary conditions are accurate.

5.1 Geometry and Fiber Content Adjustments

This section reviews adjustments made to the prototype-A FE model to incorporate more accurate material properties and geometry.

5.1.1 Reduced Fiber Content

Since material properties were a likely source of error, it was necessary to check if the fiber content value used to estimate material properties was correct. Discussions with the manufacturer and material supplier suggested that the fiber content of the beam was likely lower than originally assumed. The suggested W_f of the IM unidirectional CFRP was reduced from 72.4% to 64.1%, and the W_f of the SM unidirectional CFRP was reduced from 72.4% to 63.5% based on estimates provided form the material supplier. These lower W_f values reduced the material property values to those shown in Table 2.

Table 9 Estimated material properties for IM and SM unidirectional CFRP using ROM with reduced fiber content

Fiber Type	W_f	E11 (psi)	E22 (psi)	G12 (psi)	v12
IM UD CFRP	64.1	2.36E+07	1.09E+06	4.93E+05	0.268
SM UD CFRP	63.5	1.83E+07	1.01E+06	4.87E+05	0.269

Substituting these reduced material property values into the FE model resulted in a vertical spring rate of 751 lb/in, a lateral spring rate of 39.2 lb/in, and a torsional spring rate of 187 in*lb/°. This correlates to errors of 34.0%, 32.5%, and 27.4% for vertical, lateral, and torsional spring rates respectively.

5.1.2 Fabric Material Properties

The large remaining error prompted further adjustments to the material properties. The first two iterations of material properties used ROM. ROM is an idealized case that does not take into account any defects. Since defects are inevitable, and since the majority of the beam uses stitched fabrics instead of pure unidirectional plies, material properties for the actual fabrics needed to be obtained. These were estimated and provided by the fabric supplier. Properties for the two fabric types were provided for two different fiber content values, allowing properties for any fiber content value to be interpolated. All 0° plies were assigned the IM unidirectional fabric properties, and the 45, -45, and 90° plies were combined and assigned the SM triaxial fabric properties. The material properties provided did not include Poisson's ratio, however. Poisson's ratio for the IM unidirectional fabric was assumed to be similar to material data sheets of other unidirectional CFRP found. Poisson's ratio for the SM triaxial fabric was estimated by observing the response of the three plies of IM unidirectional CFRP in an analytical model. These properties are shown in Table 10.

Table 10 Material properties for IM unidirectional and SM triaxial fabric CFRP

Fiber Type	W_f	E11 (psi)	E22 (psi)	G12 (psi)	v12
IM UD CFRP Fabric	64.1%	21.4	2.02	0.620	0.310
SM TA CFRP Fabric	63.5%	2.54	8.33	2.56	0.232

Substituting the fabric material property values into the FE model resulted in a vertical spring rate of 690 lb/in, a lateral spring rate of 36.0 lb/in, and a torsional spring rate of 183 in*lb/°. This correlates to errors of 23.0%, 21.5%, and 24.5% for vertical, lateral, and torsional spring rates, respectively.

5.1.3 Adjusted Geometry and Layup

All models of the prototype-A beam so far have used the nominal dimensions of the pultrusion die; however, the manufactured prototype had slightly differing geometry and an altered layup due to manufacturing difficulties. The height of the beam was reduced by 1.41%, the flanges were 2.80% thinner, and were angled inward by 2.26° each. The outer corners of the flanges also had small radii, which were originally modeled as 90° corners. Manufacturing difficulties required one of the IM unidirectional plies to be removed and the ply order to be slightly rearranged. This resulted in a web layup of $\left[\text{IM-UD/SM-TA}_4/\overline{\text{IM-UD}}\right]_S$ and a flange layup of $\left[\text{IM-UD/SM-TA}_4/\overline{\text{IM-UD}_{17}}\right]_S$.

Correcting the geometry and ply layup in the FE model resulted in a vertical spring rate of 610 lb/in, a lateral spring rate of 31.5 lb/in, and a torsional spring rate of 165 in*lb/°. This correlates to errors of 8.74%, 6.55%, and 12.8% for vertical, lateral, and torsional spring rates, respectively.

5.1.4 Localized Fiber Content and Defects

To ensure the expected fiber content was being achieved, specimens were cut from different sections of the beam and sent to a lab for burn-off testing. Three total specimens were tested: one specimen from the radius, one from the web, and one from the middle of the top flange. These specimen locations are shown in Figure 18.

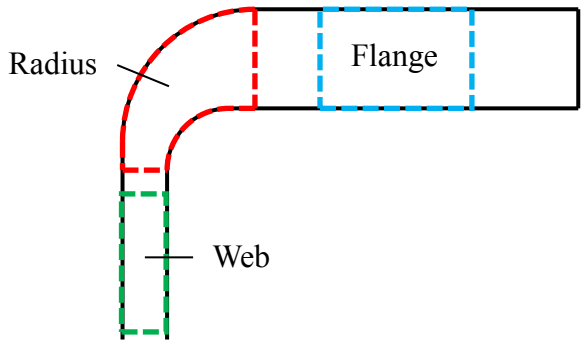

Figure 18 Specimen locations for burn-off testing

Results from the burn-off testing showed different fiber content than expected, and the material properties were adjusted accordingly. The web specimen had a W_f of 64.5%, the flange specimen had a W_f of 67.6%, and the radius specimen had a W_f of 59.2%. Since material properties can be scaled based on fiber content, properties in the web were scaled up to reflect the higher fiber content. The plies in the web that extend into the radii and flanges were also assigned these properties. W_f of the unidirectional plies in the flange center was calculated to be 69.6% in order to have a total W_f of 67.6% for the top flange. It can be assumed that the increased fiber content in the flange occurs mostly in section of unidirectional plies in the flange center, as the fibers will nest more easily than the crossing plies of the triaxial fabric. W_f of the unidirectional tow in the radius transition was calculated to be 51.0% in order to have a total W_f of 59.2% for the entire radius. Material properties in these two areas were scaled according to the new fiber content values. The low fiber content in the radius transition and high fiber content in the flange center is apparent in the microscope images in Figure 19.

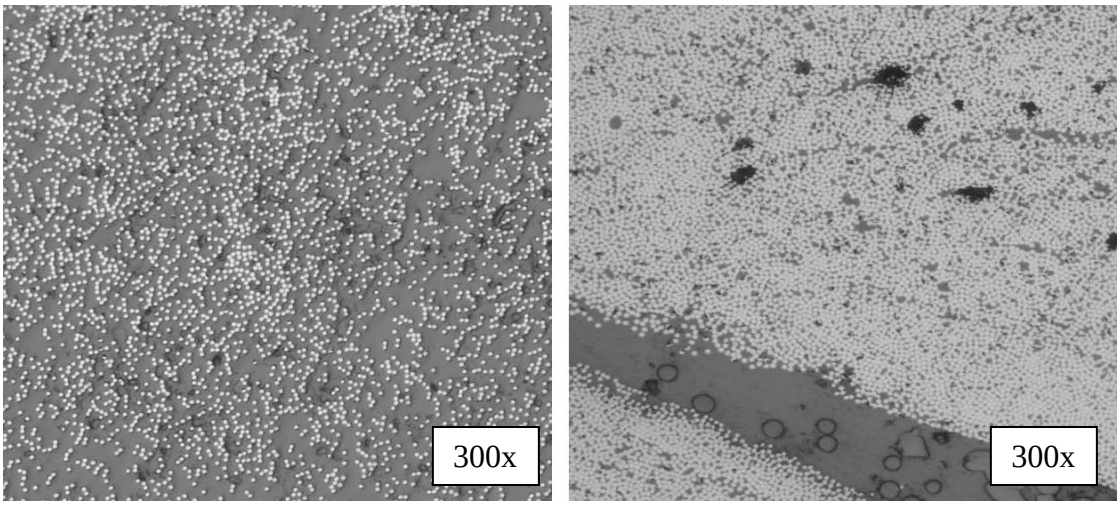

Figure 19 Microscope images showing low fiber content in the radius transition (left) and high fiber content in the flange center (right) (image courtesy of Toray Carbon Fibers America, Inc.)

Additional visual analysis revealed further defects. The unidirectional ply along the inner surface of the beam is folded in the bottom radius and terminates early. Another unidirectional ply that is supposed to part of the bottom flange center is missing. The triaxial plies that extend into each flange also terminate early. Each of these defects is shown in Figure 20.

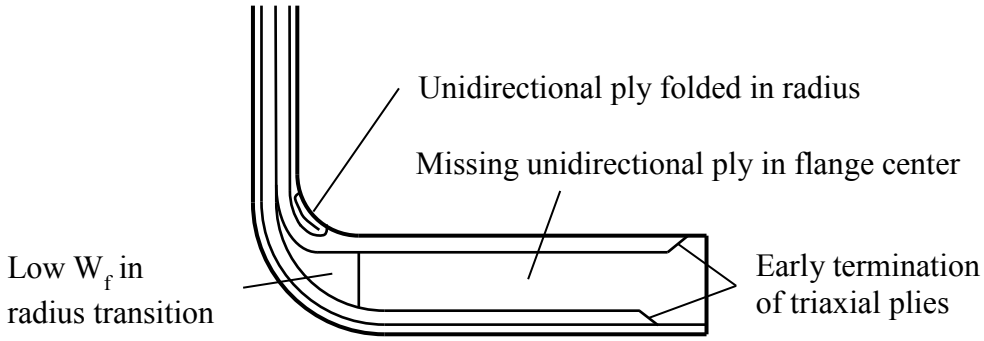

Figure 20 Diagram of defects in the bottom flange.

The FE model was adjusted to account for these flaws. Since the fiber weight for the top flange is known from the burn-off testing, the fiber weight in the bottom flange can be estimated by subtracting the weight of the missing unidirectional plies.

Doing so results in a W_f of 63.7% for the unidirectional plies in the bottom flange center. The early termination of the triaxial plies was accounted for by removing them from the ply layup in the flange tips. The fiber content in the flange tips was reduced since a known amount of fiber now occupies a larger space with the absence of the triaxial flies. The W_f of unidirectional fiber in the top flange tip was reduced to 51.7%, and the unidirectional fiber in the bottom flange tip was reduced to 47.1%. Material properties in the flange tips were scaled down to reflect the lower fiber content values. The folded unidirectional ply in the radius was modeled as two plies in the region of overlap and removed from the top surface of the bottom flange.

Incorporating the localized fiber content and defects into the FE model resulted in a vertical spring rate of 606 lb/in, a lateral spring rate of 31.6 lb/in, and a torsional spring rate of 164 in*lb/°. This correlates to errors of 8.03%, 6.85%, and 11.7% for vertical, lateral, and torsional spring rates, respectively.

5.1.5 Adjusted Localized Fiber Content

Material properties were adjusted a final time to incorporate possible errors from the burn-off testing. The manufactured prototype produced the correct thickness in the web, and since a known amount of fiber went into the web, the average W_f of the web should have been exactly 63.7%. This is different from the flanges where the total thickness was different than expected, and the unidirectional fibers in the flange centers can nest more easily. While burn-off testing is useful, it is not necessarily always reliable. If additives or the stitching do not fully burn-off, fiber content will be over reported. There was a 0.80% difference between expected fiber content in the

web and measured fiber content. Since the expected fiber content should have been achieved, this difference can be attributed to stitching and additives not fully burning off. Material properties in all locations were scaled down to reflect a W_f reduction of 0.80%.

Incorporating these changes into the model resulted in a vertical spring rate of 597 lb/in, a lateral spring rate of 31.2 lb/in, and a torsional spring rate of 162 in*lb/°. This correlates to errors of 6.38%, 5.26%, and 10.4% for vertical, lateral, and torsional spring rates, respectively.

5.1.6 Results Summary and Discussion

The prototype-A FE model went through several iterations to correct for geometry and material properties by determining localized fiber content. The results from each iteration, including the original FE model from the previous section, are shown in Table 11.

Table 11 Prototype-A FE model results summary

Prototype-A Beam Results Type	Vertical Spring Rate (lb/in)	Vertical Spring Rate Error	Lateral Spring Rate (lb/in)	Lateral Spring Rate Error	Torsional Spring Rate (in*lb/°)	Torsional Spring Rate Error
Physical Testing	561	-	29.6	-	147	-
Original FE Model	830	48.0%	43.3	46.3%	211	44.0%
Adjusted Fiber Content	751	34.0%	39.2	32.5%	187	27.4%
Fabric Properties	690	23.0%	36.0	21.5%	183	24.5%
Adjusted Geom., Layup.	610	8.74%	31.5	6.55%	165	12.8%
Localized Fiber Content 1	606	8.03%	31.6	6.85%	164	11.7%
Localized Fiber Content 2	597	6.38%	31.2	5.26%	162	10.4%

Although the FE model made significant improvements in error, material properties are still a likely source of error. Although better than using ROM, the fabric properties from the material supplier were still only estimates, as they were never physically tested for. They did not consider resin type and likely did not include defects such as cracks, voids, and matrix fiber deboning that could affect the material property values.

It is possible to determine the true material property values by testing the existing beam. The following section covers a series of tensile tests performed on specimens cut from the beam in an attempt to determine the actual material property values. These material properties can then be applied to the FE model to see if model-experiment agreement is improved.

5.2 Tensile Test Material Property Adjustments

The remaining error in the FE model from the previous section prompted a series of tensile tests to assist in determining the actual properties of the fabrics used in the prototype-A beam. This process involved cutting specimens of different orientations from different sections of the beam. These specimens underwent tensile testing to determine the overall stiffness of the specimen. Models of the tensile tests were created, and the material property inputs were adjusted until the model matches the experiment. These "backed-out" properties were then applied to the full beam FE model to see if error is reduced. This section reviews the tensile specimen testing, FE and analytical modeling, material property back-out, and application to the full beam model.

5.2.1 Tensile Specimen Testing

This section reviews the entire tensile specimen testing process. It includes the tensile specimen specifications, the experimental test setup, and the experimental results.

5.2.1.1 Tensile Specimen Specifications

Specimens of varying orientations were machined from the web and flanges of the prototype-A beam. Five orientations were machined from the web of the beam: 0, 30, 45, 60, and 90°, relative to the longitudinal axis of the beam. These specimens were 1.0 in wide, 8.0 in long, and about 0.31 in thick. Two orientations were machined from the flanges of the beam: 0 and 15°. The 0° specimens were 1.0 in wide, 8.0 in long, and about 0.75 in thick. The 15° specimens were 1 in wide, 5.70 in long, and about

0.75 in thick. The narrowness of the flange caused the 15° specimens to be shorter than the other specimens and prevented larger angled specimens from being cut.

5.2.1.2 Experimental Test Setup

The specimens underwent testing on a tension tester. The tension tester machine was an Instron model 5500R. Strain was measured using an Instron 2630-100 series clip-on extensometer with a 1 in gage length. Force was measured with a 100 kN load cell. The geometry of the specimens was measured with digital calipers. Six 0° and three 30, 45, 60, and 90° web specimens were each tested using model 2716-002 grips with 1 in wide jaw faces. Four 0° and five 15° flange specimens were each tested, but required custom fixturing. The jaw faces could not accept specimens wider than 0.5 in, so a clevis fixture was machined from steel. A 3/8 inch steel dowel pin connected the clevises to the ends of the flange specimens, and the tangs of the clevises fit into the jaw faces. Figure 21 shows a 15° flange specimen in the clevis fixture. The specimens were loaded at a rate of 0.05 in/min, and stress and strain data were recorded every 0.1 seconds.

Figure 21 15° flange specimen in clevis fixture

5.2.1.3 Tensile Testing Results Summary and Discussion

The tensile specimen testing results are summarized in Table 12. The table includes the average specimen stiffness for each specimen location and orientation. It also

includes the standard deviation of the stiffnesses for each specimen type as well as the standard deviation's percentage of the average stiffness. The flange specimens had considerable more scatter than the web specimens. All of the stress versus strain plots can be seen in APPENDIX B.

Table 12 Prototype-A tensile specimen testing results

Specimen Location and Angle	Average Physical Stiffness (psi)	Physical Stiffness Standard Deviation (psi)	Standard Deviation Percentage
Web, 0°	7.58E+06	3.53E+05	4.65%
Web, 30°	5.92E+06	2.71E+05	4.57%
Web, 45°	5.66E+06	3.01E+04	0.532%
Web, 60°	5.65E+06	2.56E+05	4.53%
Web, 90°	5.71E+06	9.17E+04	1.61%
Flange, 0°	1.57E+07	1.26E+06	8.05%
Flange, 15°	8.76E+06	1.19E+06	13.5%

Similar to the overall beam testing, FE and analytical models were needed in order to compare the specimens to the expected theoretical stiffness and to allow for material property back-out. The following section covers this process.

5.2.2 FE and Analytical Modeling Tensile Specimen Testing

FE and analytical models of the tensile specimen testing were created. This allows the material property inputs of the models to be varied in order to determine the actual values of the material properties, which can then be plugged back into the full beam model. It also allows a comparison between experimental results and model results to see if similar error is seen as with the full beam model and experiment. This section

covers the FE and analytical modeling of the tensile tests and their results, the process of backing out material properties, and the application of the material properties back into the full beam model.

5.2.2.1 FE Modeling of Tensile Specimen Testing

FE models of the tension tests were generated to simulate the loading and boundary conditions of the physical tests. Continuum shell elements were used for each ply of the web specimens. This allows the model to incorporate the shear lag that exists when loading specimens with jaw face style grips. The surfaces in contact with the jaw faces were assigned a fixed boundary condition on one end and a displacement boundary condition on the other. Reaction force was recorded and converted to average stress, and strain was measured over a 1 in section at the same location as the extensometer used in the physical test. An image of the loaded web specimen FE model is shown in Figure 22.

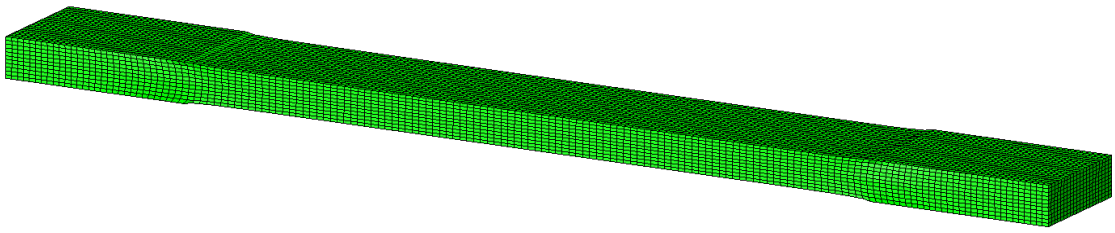

Figure 22 FE model of loaded 0° web specimen (deformation scale factor: 800)

The flange specimens were modeled similarly. However, due to the increased thickness, the center section of unidirectional plies has one continuum shell element for every two plies. The steel dowel pins of the clevis fixture were modeled with steel sections that share some nodes with the flange specimen. The tips of one steel section

were assigned a fixed boundary condition, and the tips of the other steel section were assigned a displacement boundary condition, similar to how the clevis applies forces to the steel pins. Reaction force was recorded and converted to average stress, and strain was measured over a 1 in section at the same locational as the extensometer. An image of the loaded flange specimen FE model is shown in Figure 23.

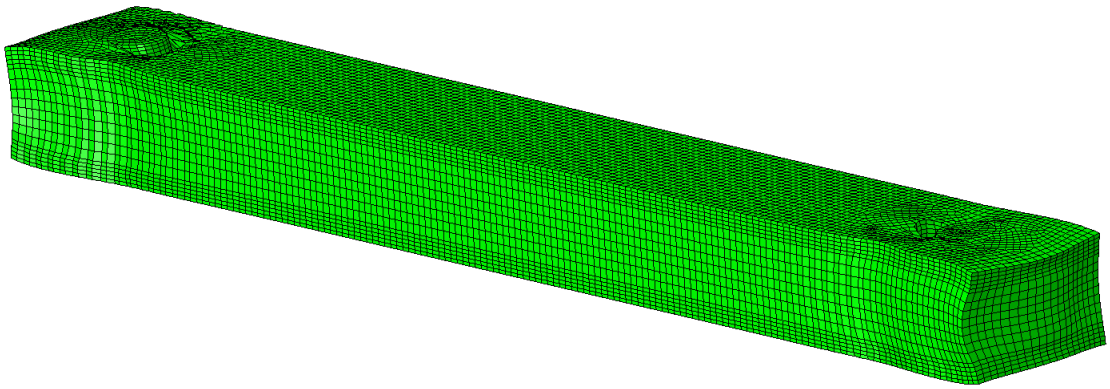

Figure 23 FE model of loaded 0° flange specimen (deformation scale factor: 800)

5.2.2.2 Analytical Modeling of Tensile Specimen Testing

An analytical model of the tensile specimen testing was created to compare to the FE models and physical testing. A MATLAB program was written based on composite lamination theory that models each specimen's response to an axial load. The analytical model, however, does not account for the edge effects or loading conditions of the physical test.

5.2.2.3 Tensile Test Modeling Results

The results from the tensile specimen testing models are summarized in Table 13. The specimen stiffness for FE and analytical models are given for each specimen type, as well as the error between the model and experimental results.

Table 13 Tensile specimen testing results summary

Specimen Location and Angle	Physical Stiffness (psi)	FEA Stiffness (psi)	FEA Stiffness Error	Analytical Stiffness (psi)	Analytical Stiffness Error
Web, 0°	7.58E+06	7.29E+06	-3.85%	7.29E+06	-3.84%
Web, 30°	5.92E+06	5.83E+06	-1.57%	6.11E+06	3.11%
Web, 45°	5.66E+06	5.69E+06	0.49%	5.83E+06	3.01%
Web, 60°	5.65E+06	6.21E+06	9.94%	6.22E+06	10.2%
Web, 90°	5.71E+06	7.48E+06	30.9%	7.61E+06	33.3%
Flange, 0°	1.57E+07	1.65E+07	5.16%	1.67E+07	6.18%
Flange, 15°	8.76E+06	8.47E+06	-3.34%	9.75E+06	11.2%

5.2.3 Material Property Back-out

Before material properties could be backed-out from the tensile test models, agreement was necessary between the analytical and FE models. The models had some disagreement for the angled specimens. Since the FE models were able to more accurately model the boundary and loading conditions of the tensile tests, the FE model results can be assumed to be more accurate. However, the optimization technique used to back-out material properties is a built in MATLAB function and will only work for the analytical model. To compensate for this, correction factors were applied in the analytical model for each specimen orientation and location in order to match the FE model results. These offset factors are shown in Table 14.

Table 14 Offset factors applied to analytical tensile test model to match FEA results

Specimen Location and Angle	FEA Stiffness (psi)	Analytical Stiffness (psi)	Correction Factor
Web, 0°	7.29E+06	7.29E+06	1.000
Web, 30°	5.83E+06	6.11E+06	0.955
Web, 45°	5.69E+06	5.83E+06	0.976
Web, 60°	6.21E+06	6.22E+06	0.998
Web, 90°	7.48E+06	7.61E+06	0.982
Flange, 0°	1.65E+07	1.67E+07	0.990
Flange, 15°	8.47E+06	9.75E+06	0.869

The optimization technique was run to back-out the critical material properties from the analytical model with the Poisson's ratios held constant. The MATLAB function fminsearch was used to minimize an error term in the analytical model. The error term was the sum of the absolute values of the stiffness error between the model results and experimental results. The function fminsearch varied E11, E22, and G12 for both fabric types. Poisson's ratios were held constant, as fminsearch was outputting unrealistic values when they were allowed to vary. Holding these values constant is valid since Poisson's ratio has very little effect on the overall spring rate of the beam model. A sensitivity study that varies the four material property values for each fabric type by 25% was conducted. The results showed that of the eight total material properties, the Poisson's ratios have the smallest effect on spring rate. The percentage change in spring rate versus the material property varied is shown in Figure 24. The largest percent change in spring rate caused by a change in Poisson's ratio was 0.39%.

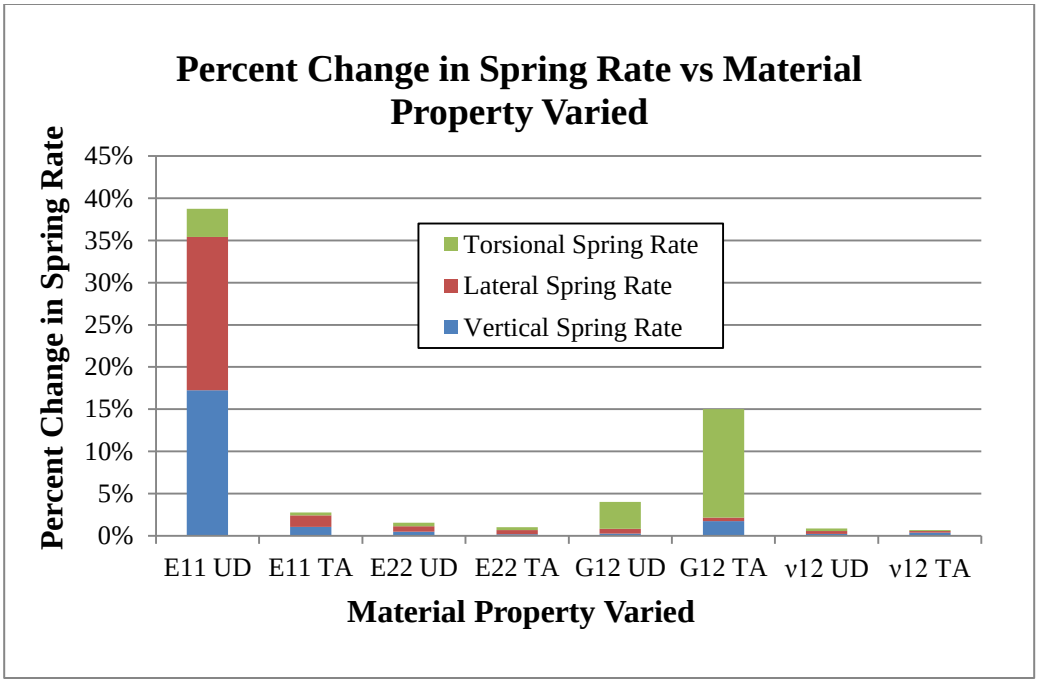

Figure 24 Percent change in spring rate vs. material property varied

Using the backed out material properties from fminsearch, the error in the analytical model was greatly reduced. The total error was reduced from $3.88*10^6$ psi to $2.01*10^5$ psi, a 95% reduction. The backed-out material properties that give this reduced error are shown in Table 15. Table 16 shows the stiffness results from the analytical model using the backed-out material properties compared to the nominal material properties. These results include the FEA correction factor.

Table 15 Backed-out material properties from analytical model

Fiber Type	E11 (psi)	E22 (psi)	G12 (psi)	ν12
IM UD CFRP Fabric	2.10E+07	1.51E+06	8.06E+05	0.310
SM TA CFRP Fabric	3.07E+06	6.78E+06	2.70E+06	0.232

Table 16 Analytical stiffness with nominal material properties compared to backed-out material properties

Specimen Location and Angle	Physical Stiffness (psi)	Analytical Stiffness, Nominal Properties (psi)	Analytical Stiffness, Nominal Properties Error	Analytical Stiffness, Backed-out Properties (psi)	Analytical Stiffness, Backed-out Properties Error
Web, 0°	7.58E+06	7.29E+06	-3.88%	7.58E+06	0.00%
Web, 30°	5.92E+06	5.82E+06	-1.78%	6.06E+06	2.31%
Web, 45°	5.66E+06	5.67E+06	0.27%	5.66E+06	0.00%
Web, 60°	5.65E+06	6.20E+06	9.85%	5.65E+06	0.06%
Web, 90°	5.71E+06	7.50E+06	31.3%	5.77E+06	1.04%
Flange, 0°	1.57E+07	1.65E+07	5.12%	1.57E+07	-0.01%
Flange, 15°	8.76E+06	8.45E+06	-3.61%	8.76E+06	-0.01%

5.2.4 Backed-out Material Properties Applied to Beam FE Model

The backed-out material properties were applied to the prototype-A beam FE model. The material properties values for the IM unidirectional CFRP in the flange tips and radius transition were scaled from the backed-out properties to match the appropriate fiber content values that were previously determined. The beam stiffness results are shown in Table 17.

Table 17 Prototype-A FE model results for backed-out material properties

Prototype-A Beam Results Type	Vertical Spring Rate (lb/in)	Vertical Spring Rate Error	Lateral Spring Rate (lb/in)	Lateral Spring Rate Error	Torsional Spring Rate (in*lb/°)	Torsional Spring Rate Error
Physical Testing	561	-	29.6	-	147	-
Backed-out Properties	613	9.27%	31.9	7.67%	170	16.1%

The results in Table 17 show more error than the last FE model in the geometry and fiber content adjustment section. Error in vertical spring rate increased from 6.38% to 9.27%, lateral spring rate increased from 5.26% to 7.67%, and torsional spring rate error increased from 10.4% to 16.1%.

The source of the increased error is likely due to difficulties during the tensile specimen testing. The knife edges on the clip-on extensometer were not sufficiently sharp to attach securely to the sides of the tensile specimens. During some tests, the extensometer would slip along on the specimen, causing a sharp drop in strain output. In this case, the specimen would be re-tested, or the data after the strain drop would be ignored. It is also possible that there was more constant gradual slipping of the extensometer during the entirety of the tests. Since the extensometer tended to slip in the direction of less strain, the overall strain in the specimen would go underreported, causing the overall stiffness to be over reported. This caused the backed-out material properties to be too high, leading to the increase in error of the prototype-A FE model.

5.3 Boundary Condition Checking

The last likely source of error in the prototype-A FE model is the boundary condition at the rear of the beam. It was originally assumed that the entire area of the web clamped by the steel plate would be constrained. However, it is possible that some slippage could occur in the areas away from the bolts. It is also possible that other inaccuracies exist in the prototype-A FE model.

In order to check if there is an inherent error in the FE modeling process, a steel c-channel beam of similar overall size was tested in the same configuration as the

prototype-A beam. An FE model of the steel beam was created in the exact same manner as the prototype-A beam. Since material properties and geometry for steel are well known, it can be assumed that any error in the model is due to boundary conditions or any other inherent inaccuracies in the model. The experimental results of the steel beam compared to the steel beam FE model are shown in Table 18.

Table 18 Steel c-channel beam experimental and FE model results

Steel C-Channel Beam Results Type	Vertical Spring Rate (lb/in)	Vertical Spring Rate Error	Lateral Spring Rate (lb/in)	Lateral Spring Rate Error	Torsional Spring Rate (in*lb/°)	Torsional Spring Rate Error
Physical Testing	554	-	38.7	-	149	-
FE Model	550	-0.783%	39.3	1.53%	167	12.6%

The steel beam showed considerably less overall error than the prototype-A beam. Error for vertical and lateral bending was negligible, with values of -0.78% and 1.53%, respectively. Torsion, however, was off by a significant amount of 12.6%. This greater increase in torsional error could explain why torsional error of the prototype-A beam was significantly higher than vertical and lateral bending. Although slight differences in size and geometry prevent an exact direct comparison between the error in the steel beam and the prototype-A beam, it can be assumed that any inherent error in the FE model did not significantly affect the vertical or lateral bending spring rates.

5.4 Summary

The sources of error between the prototype-A beam FE model and physical testing have been identified. Inaccurate material properties was the largest source of error in

the prototype-A FE model. Using ROM to estimate material properties greatly over predicted the stiffness of the materials. Material properties in the model were also affected by high estimates of fiber content. Using corrected localized fiber content and material properties from the fabric supplier greatly reduced the error in the model. The manufactured prototype also had significantly altered geometry than originally intended. The angled flanges were likely due to residual stresses that occurred during the curing process. Changes in ply layup, missing plies, and folded plies also had negative impacts on the model. The higher torsional error could also be partially attributed to inherent error in the FE model when trying to model the specific boundary and loading conditions of the physical testing.

It is possible to account for these errors when designing new composite beams. It is important to use the best estimates of material properties that are available and, in the case of the prototype-A beam, they were the properties provided by the material supplier. It is also important to assume a realistic fiber content, which has been around 64% by weight for a pultruded CFRP beam. Accounting for defects such as reduced geometry and ply changes is more difficult, as these are often manufacturing issues that the original designer may not be aware of. Using a buffer on the stiffness targets can help compensate for anticipated defects. In the case of the prototype-A beam, this buffer is around 23%.

6 Material Selection for Prototype-B Beam Design

After analyzing the prototype-A beam, new designs were generated using the MTLB based MATLAB code to compare the cost and performance of different composite materials. Cost and performance are measured by how much one has to pay for weight savings. The exact metric is the cost of the composite beam relative to the cost of the steel beam, divided by the weight savings ratio of the composite beam. This is more clearly shown in the equation below:

$$\text{CostPerWeightSavings} = \frac{(\text{CompositeCost}/\text{SteelCost})}{(\text{WeightSaved}/\text{SteelWeight})}$$

The different materials compared were standard modulus carbon fiber, intermediate modulus carbon fiber, glass fiber, and core materials. The goal is to see if using the alternate materials of glass fiber or core materials will yield a *manufactured* cost ratio per weight-saved ratio of 13.5. A *raw material* cost ratio is also discussed in this section. This section reviews the stiffness targets of the prototype-B design, material properties, material costs, how the materials perform in isolated loading cases, and the prototype-B designs.

6.1 Stiffness Targets

New stiffness targets were generated for prototype-B beam designs. These targets were obtained by calculating the effective vertical bending, lateral bending, and torsional stiffnesses of a steel beam, and then applying buffers to compensate for the expected defects seen in the CFRP prototype. The buffers chosen were 23.0%, 21.5%, and 24.5%, which were the error values for the prototype-A beam for vertical, lateral,

and torsional spring rates, respectively, after the fabric properties were used. The buffered stiffness targets are shown below in Table 19.

Table 19 Stiffness targets for prototype-B designs

Loading Mode	Stiffness (lb*in^2)
Effective Vertical Bending	2.23E+09
Lateral Bending	1.63E+08
Torsion	1.68E+06

6.2 Material Properties

The prototype-B beam designs consider three different types of fiber. These fibers are standard modulus carbon, intermediate modulus carbon, and E-glass (EG). The standard modulus fiber considered in the prototype beam was limited to the triaxial fabric, but was expanded to unidirectional fabric and a different triaxial fabric for the next designs. The newer triaxial fabric has a higher ratio of 45/-45° cross ply layers to 90° layers than the original triaxial fabric. This allows for an increase in shear stiffness at the expense of transverse stiffness. The intermediate modulus carbon fibers remained available only as unidirectional fabrics. E-glass fibers were considered in both unidirectional and triaxial fabric configurations. Material properties were obtained from the fabric supplier, with the exception of the standard modulus unidirectional fabric. These fabric properties were estimated based on the known fiber and fabric properties of the intermediate modulus carbon fiber, scaled down to fit the known properties of the standard modulus carbon fiber. These five materials and their major properties are shown in Table 20.

Table 20 Material properties considered for new beam designs

Fiber and Fabric Type	E11 (psi)	E22 (psi)	G12 (psi)	v12	ρ (lb/in^3)
SM UD CFRP	1.68E+07	1.75E+06	6.20E+05	0.310	0.0553
SM TA CFRP	2.74E+06	6.63E+06	2.98E+06	0.232	0.0553
IM UD CFRP	2.14E+07	2.02E+06	6.20E+05	0.310	0.0553
EG UD GFRP	5.34E+06	1.62E+06	7.70E+05	0.310	0.0672
EG TA GFRP	2.25E+06	3.20E+06	1.40E+06	0.232	0.0686

Material properties of the core materials are assumed to be idealized. The goal of investigating core materials is to see if the best case scenario will yield the target cost per weight-savings value of 13.5. The mechanical properties are assumed to be negligible compared to the FRPs. However, the density of the core material is assumed to be zero in order to get the best case result.

6.3 Material and Manufacturing Costs

Material and manufacturing costs were estimated in order to compare the cost and performance of the five materials. These costs were obtained through discussions with the material suppliers and the prototype-A beam manufacturer. Material costs include the raw fiber cost plus the additional cost of stitching them together to form fabrics. It also includes the raw material costs of the resin. Raw material cost of the core material is assumed to be zero in order to get the best case scenario results. The manufacturing costs were based on the amount paid for the prototype-A beam manufacture. It includes a new pultrusion die, set up time, labor for each beam, and post machining operations. It also includes the material scrap rate and material discounts when buying

in bulk for large beam orders. For the manufactured cost ratios discussed later in this section, an order of 2000 beams is assumed.

6.4 Material Comparison for Isolated Loading Scenarios

Before the prototype-B beam designs were created, the previously described materials were compared in isolated loading scenarios to determine the *raw material* cost per weight-savings of each material type. *Manufactured* cost per weight-savings was not used since many of these models have unrealistic geometry. This section reviews the loading cases of axial loading, vertical bending, lateral bending, and torsion.

6.4.1 Material Comparison for Axial Loading

The first loading scenario for material comparison to steel is axial loading. For this case, IM and SM unidirectional CFRP and E-glass unidirectional GFRP were compared to nominal properties of steel. The weight and axial stiffness of a 12 in long steel bar with a 1 in^2 cross section was calculated. An equivalently stiff bar of each composite material type was then compared to the steel bar. The weight savings and cost ratios are shown in Table 21.

Table 21 Material comparison for axial loading

Material	Axial Stiffness (psi)	Weight Saved Ratio	Raw Material Cost Ratio	Raw Material Cost Ratio per Weight Savings Ratio
IM UD CFRP	2.90E+07	0.736	24.1	32.8
SM UD CFRP	2.90E+07	0.664	21.4	32.2
EG UD GFRP	2.90E+07	-0.285	20.3	-

The results in Table 21 show that the two carbon fiber types are comparable and that glass fiber is not a feasible alternative. The SM unidirectional CFRP slightly outperformed the IM CFRP in cost per weight-saved. The lower cost of SM carbon fiber barely overcame the fact that a greater amount of it was needed to match the stiffness of the steel bar. Although the cheapest, the amount of GFRP required to match the stiffness of the steel bar was actually greater than the weight of the steel bear, hence the negative weight saved. The cost of the GFRP becomes unnecessary since one would be paying for extra weight instead of weight savings.

6.4.2 Material Comparison for Vertical Bending

The next loading scenario for the material comparison is vertical bending. The vertical bending stiffness target of the prototype-B beam was used as a target for the isolated loading case. A MATLAB program based on MTLB was used to design three beams with material in the flanges only, an optimized material location for vertical bending stiffness. Each unidirectional material type was added into the flanges until the vertical bending stiffness target was met. Since no material was placed in the web, shear deformation was ignored. The weight savings and raw material cost ratios are shown in Table 22.

Table 22 Material comparison for vertical bending

Material	$EI_{vertical}$ ($lbs*in^2$)	Weight Saved Ratio	Raw Material Cost Ratio	Raw Material Cost Ratio per Weight Savings Ratio
IM UD CFRP	2.23E+09	0.854	3.08	3.60
SM UD CFRP	2.23E+09	0.814	2.72	3.35
EG UD GFRP	2.23E+09	0.293	2.56	8.7

The results in Table 22 show similar results to the previous loading scenarios. Again, SM unidirectional CFRP slightly outperforms IM unidirectional CFRP. In the vertical bending case, weight savings was achieved with GFRP, although the cost of the weight savings was higher than either CFRP. However, this was only the case since the material location was optimized to only the flanges, but the steel beam being compared to has material in the web as well. So although it is useful to compare the FRP materials to each other, it does not provide a realistic comparison to steel.

6.4.3 Material Comparison for Lateral Bending

The third loading scenario for the materials comparison is lateral bending. The lateral bending stiffness target of the prototype-B beam was used as a target for the isolated loading case. Similar to vertical bending, a MATLAB program based on MTLB was used to design three beams, but material was mostly evenly distributed along the entire profile. Material was added along the profile until it almost met the lateral bending stiffness. Then a small amount of material was added into the flanges only to meet the target exactly. The weight savings and raw material cost ratios are shown in Table 23.

Table 23 Material comparison for lateral bending

Material	$EI_{lateral}$ ($lbs*in^2$)	Weight Saved Ratio	Raw Material Cost Ratio	Raw Material Cost Ratio per Weight Savings Ratio
IM UD CFRP	1.66E+08	0.710	26.6	37.4
SM UD CFRP	1.66E+08	0.630	23.6	37.4
EG UD GFRP	1.66E+08	-0.314	20.7	-

Again, the results in Table 23 show similar results to the previous loading scenarios. SM and IM unidirectional CFRP performed identically. Since the material was distributed similarly to the steel beam, the unidirectional GFRP design was heavier than the steel beam, unlike the optimized location of the vertical bending scenario. Because of this, it does not make sense to list the cost per weight-savings.

6.4.4 Material Comparison for Torsion

Lastly, materials were compared in a torsional loading scenario. Since the triaxial fabrics have high shear stiffnesses, and torsion is a shear loading scenario, it makes sense to compare triaxial materials, as they carry the majority of the shear load. SM triaxial CFRP was compared to E-glass triaxial GFRP in two different analytical models. Triaxial fabric was placed along the entire profile until the torsional stiffness was almost met. Additional fabric was placed in the flanges until the exact torsional stiffness was reached. The weight savings and raw material cost ratios are shown in Table 24.

Table 24 Material comparison for torsion

Material	$GJ_{torsional}$ ($lbs*in^2$)	Weight Saved Ratio	Raw Material Cost Ratio	Raw Material Cost Ratio per Weight Savings Ratio
SM TA CFRP	1.67E+06	0.650	22.0	33.9
EG TA GFRP	1.67E+06	0.440	8.73	19.8

The results from Table 24 show that triaxial GFRP outperforms triaxial CFRP in a purely torsional loading scenario. However, this is likely due to the geometry of the GFRP design as opposed to the actual material properties. The polar moment of inertia is highly dependent on the thickness of the cross-section profile as shown in the polar moment of inertia equation in section 2.2.2. Since the shear stiffness of the triaxial GFRP is much lower than the triaxial CFRP, a much larger thickness is required to obtain similar stiffness. Since polar moment of inertia is a function of the thickness cubed, the thicker GFRP design will perform better than CFRP, but only based on the geometry, and not material properties. CFRP would likely outperform GFRP if a spacer was used to increase the thickness between triaxial layers. In order to get a better comparison, glass must be compared to carbon in designs that meet all beam stiffness requirements, which is covered in the following section.

6.5 Prototype-B Beam Designs

Eight prototype-B designs were created using the previously described materials. This section reviews the ply layup creation process, geometry constraints, the layups and materials for each design, and the cost and performance results of each design.

6.5.1 Ply Layup Creation

Ply layups for the prototype-B designs were created manually using the MATLAB program based on MTLB. The program is similar to the one shown in APPENDIX A, but includes cost and weight information and easier geometry and ply manipulation. To create the ply layup, three main effects are considered. To increase vertical bending spring rate, add unidirectional plies to the flange centers. This will also increase lateral bending spring rate, as well as torsional spring rate, due to spacing the triaxial plies further apart. To increase lateral bending spring rate, add unidirectional plies to the entire profile. This will also increase vertical bending spring rate, as well as torsional spring rate, if the plies are added in between the triaxial plies. To increase torsional spring rate, add triaxial plies to the entire profile, as close to the outside of the layup as possible. This will also increase vertical bending stiffness by resisting shear deformation. Because all of these effects are interconnected, a great amount of manual tweaking was required to match the stiffness targets as closely and as weight efficiently as possible.

6.5.2 Geometry Constraints

The prototype-B beam designs also had different geometry constraints than prototype-A. The overall height was reduced to from 11.66 to 11.13 inches to prevent attaching components from having to being modified to accept the taller beam. However, designs with a height of 12.13 inches were also be explored to see if significant cost savings can be achieved by having a taller beam, which could offset the costs of having to modify the attaching components. The width of the beam was allowed to

increase from 3.44 to 3.70 inches. The web thickness limit remained at 0.50 in. The inner height of the web that needs to be flat for attaching components was reduced from 9.0 in to 8.5 in. Adding 0.5 in radii to the top and bottom of the web brings the total inner height between the flanges to 9.5 in. Since the overall height is reduced, the allowable flange thickness drops from 0.83 to 0.81 in for the preferred geometry constraints. These constraints are shown in Table 25.

Table 25 Geometry constraints for prototype-B beam designs

Dimension	Prototype-A Value (in)	Prototype-B Preferred Value (in)	Prototype-B Maximum Value (in)
Overall Height	11.66	11.13	12.13
Overall Width	3.44	3.70	3.70
Web Thickness	0.50	0.50	0.50
Web Height	9.00	8.50	8.50
Flange Thickness	0.83	0.81	1.31

6.5.3 Prototype-B Beam Designs and Results

Ten different beam layups were created from the new set of materials. The first four meet the preferred geometry constraints, and the last six meet the maximum geometry constraints. The stiffnesses, weight savings ratio, manufactured cost ratio, and manufactured cost ratio per weight savings ratio for each beam design are shown in Table 26. The prototype-A beam model is also shown in the table as a reference to see if improvement has been made for the prototype-B designs, although different stiffness targets and geometry constraints are used. The following sections describe

each of the prototype-B beam designs and discuss the use of IM vs. SM unidirectional CFRP, triaxial GFRP, unidirectional GFRP, and core materials in the web and flanges.

Table 26 Prototype-B beam design results that meet the preferred geometry constraints

Beam Type	Effective $EI_{vertical}$ ($lbs*in^2$)	$EI_{lateral}$ ($lbs*in^2$)	$GJ_{torsional}$ ($lbs*in^2$)	Weight Savings Ratio	Manuf. Cost Ratio	Manuf. Cost Ratio per Weight Savings Ratio
Prototype-B Targets	2.23E+09	1.63E+08	1.68E+06	-	-	13.5
Prototype-A	2.21E+09	1.18E+08	1.80E+06	0.643	16.9	26.3
Prototype-B-1	2.24E+09	1.64E+08	1.73E+06	0.639	16.5	25.8
Prototype-B-2	2.33E+09	1.63E+08	1.76E+06	0.656	17.0	26.0
Prototype-B-3	2.44E+09	1.63E+08	1.68E+06	0.600	16.0	26.7
Prototype-B-4	2.57E+09	1.69E+08	1.68E+06	0.618	17.8	28.8
Prototype-B-5	2.25E+09	1.72E+09	1.80E+06	0.566	16.9	29.9
Prototype-B-6	2.41E+09	1.63E+08	1.89E+06	0.447	15.0	33.7
Prototype-B-7	2.27E+09	1.65E+08	1.69E+06	0.588	15.9	27.0
Prototype-B-8	2.23E+09	1.66E+08	1.73E+06	0.657	16.3	24.8
Prototype-B-9	2.27E+09	1.63E+08	1.68E+06	0.636	15.2	24.0
Prototype-B-10	2.24E+09	1.63E+08	1.69E+06	0.701	15.9	22.7

6.5.3.1 IM versus SM Unidirectional CFRP

The first two prototype-B designs compare the use of IM and SM unidirectional CFRP in a full beam design that meets the preferred geometry constraints. The prototype-B-1 design has a web layup of $\left[\text{SM-UD/SM-TA}_3\text{/SM-UD}_2\right]_S$ and a flange layup of $\left[\text{SM-UD/SM-TA}_3\text{/SM-UD}_2\text{/}\overline{\text{IM-UD}_{18}}\right]_S$. The prototype-B-2 layup uses IM instead of SM unidirectional CFRP, resulting in a web layup of $\left[\text{IM-UD/SM-TA}_3\text{/IM-UD}\right]_S$ and

a flange layup of $\left[\text{IM-UD/SM-TA}_3/\overline{\text{IM-UD}_{23}}\right]_S$. Like the isolated loading cases, SM unidirectional CFRP performs slightly better than IM unidirectional CFRP when considering cost per weight-saved, with values of 25.8 versus 26.0, respectively. However, the difference is almost negligible, and using IM CFRP yields a higher overall weight savings ratio, with values 17.0 versus 16.5. Both designs out perform the prototype-A design.

Prototype-B-3 and prototype-B-4 also compare IM and SM unidirectional CFRP but with the maximum geometry constraints. Because prototype-B-3 has looser geometry constraints, the flange thickness was allowed to increase, which allowed the use of SM carbon fiber exclusively. The prototype-B-3 design has a web layup of $\left[\text{SM-UD}_2/\text{SM-TA}_3/\text{SM-UD}_2\right]_S$ and a flange layup of $\left[\text{SM-UD}_2/\text{SM-TA}_3/\overline{\text{SM-UD}_{20.4}}\right]_S$. Prototype-B-4 has a web layup of $\left[\text{IM-UD/SM-TA}_4/\text{IM-UD}_2/\overline{\text{IM-UD}_5}\right]_S$ and a flange layup of $\left[\text{IM-UD/SM-TA}_4/\text{IM-UD}_2/\overline{\text{IM-UD}_{16.8}}\right]_S$. Again, the SM carbon fiber design has a lower cost per weight saved than IM carbon fiber, with values of 26.7 and 28.8, respectively. The IM carbon fiber design however saves more weight than the SM carbon fiber design, with values of 0.618 and 0.600, respectively.

Increasing the height of the beam did not help the overall cost per weight savings for these two types of designs. The highest cost per weight-savings value of the preferred geometry constraints is 26.0, and the lowest cost per weight-savings value of the maximum geometry constraints is 26.7. This is caused by the need to meet

the lateral and torsional stiffness requirements. The original thought was that an increased height would allow more efficient vertical bending stiffness, allowing the reduction of plies used in the flanges. While this is true, removing plies in the flanges decreases the lateral bending stiffness and torsional stiffness. The torsional stiffness relies on the spacing effect of the flange center unidirectional plies to move the triaxial plies away from the mid-plane. In order to meet these stiffness targets, material was not able to be removed from the beam. The increased height actually increased the overall weight of the beam since there was now more volume in the web. The lateral and torsional stiffness requirements were still met, but the vertical bending stiffness was unnecessarily exceeded.

6.5.3.2 E-Glass Triaxial GFRP

Prototype-B-5 looks at the use of triaxial GFRP under the preferred geometry constraints, and the results are unfavorable. The prototype-B-3 design has a web layup of $\left[\text{IM-UD/EG-TA}_2\text{/SM-TA}_2\text{/}\overline{\text{IM-UD}_4}\right]_S$ and a flange layup of $\left[\text{IM-UD/EG-TA}_2\text{/SM-TA}_2\text{/}\overline{\text{IM-UD}_{20}}\right]_S$. The shear stiffness of the glass triaxial is not high enough to be used by itself and still meet the geometry constraints, so two SM carbon triaxial plies were needed as well. The cost per weight-savings ratio is considerably higher (29.9) than the prototype-A design (26.3) and both of the first two prototype-B designs (25.8, 26.0). Unlike the isolated loading cases, prototype-B-5 shows that using glass triaxial fabric increases the cost per weight-savings compared to SM carbon triaxial fabric used in prototype-B-1 and prototype-B-2 designs.

Prototype-B-6 looks at the use of triaxial GFRP in the maximum geometry constraints and, again, the results are unfavorable. Since the flanges are allowed to be thicker in this configuration, more triaxial GFRP was able to be used. Also, SM unidirectional CFRP was used for all unidirectional plies instead of IM CFRP. The web has a layup of $\left[\text{SM-UD}_4/\text{EG-TA}_4\right]_S$ and a flange layup of $\left[\text{SM-UD}_4/\text{EG-TA}_4/\overline{\text{SM-UD}_{17}}\right]_S$. The extra amount of glass fiber causes this beam design to be the worst so far. The cost per weight-savings ratio is the highest at 33.7. The results from these two beams show that triaxial GFRP does not reduce the cost per weight-savings.

6.5.3.3 E-Glass Unidirectional GFRP

Prototype-B-7 looks at the use of unidirectional GFRP under the maximum geometry constraints, and the results are unfavorable. The amount of unidirectional GFRP required to have a useful effect was too large to fit within the preferred geometry constraints. The design has a web layup of $\left[\text{IM-UD}_3/\text{SM-TA}_2\right]_S$ and a flange layup of $\left[\text{IM-UD}_3/\text{SM-TA}_2/\text{IM-UD}_5/\overline{\text{EG-UD}_{15}}\right]_S$. The use of unidirectional GFRP causes a higher cost per weight-savings ratio (27.0) than prototype-A and both of the first two prototype-B designs. It did, however, out perform the all-CFRP maximum geometry constraint designs prototype-B-3 and prorotype-B-4. However, this is a result of the spacing effect the GFRP had rather than its mechanical properties. This effect is discussed in the following sections.

6.5.3.4 Core Material in the Web

Prototype-B-8 looks at the use of a core material in the web of the beam under the preferred geometry constraints, and the results are favorable, but unrealistic. Adding a core material to the web allows increased spacing between the triaxial plies, which increases the torsional stiffness of the beam. By increasing torsional stiffness geometrically, fewer triaxial plies need to be used, which decreases the total cost and weight of the beam. Using a core material does not provide a significant benefit to either bending stiffness. The layup in prototype-B-8 is comparable to prototype-B-1, but with a 0.22 in thick "air" core in the center of the web. The prototype-B-8 design has a web layup of $\left[\text{SM-UD/SM-TA}_2\text{/SM-UD}_2\text{/core}\right]_S$ and a flange layup of $\left[\text{SM-UD/SM-TA}_2\text{/SM-UD}_2\text{/}\overline{\text{IM-UD}_{19.2}}\right]_S$. However, only four SM carbon triaxial plies were needed due to the increased torsional stiffness from the spacing. Additional IM carbon unidirectional plies were needed in the flanges to compensate for the reduced average shear stiffness in the web due to the drop in SM carbon triaxial ply count. The cost per weight-savings performance is the lowest of any design so far, with a value of 24.8.

However, these results are unrealistic. Cost and density were assumed to be zero. In reality, the core would have a significant weight and cost, although much smaller than the FRPs. Adding a core material into the pultrusion process would also increase the manufacturing costs, as it would not be as continuous of a process as adding in reels of tow or fabric.. The biggest obstacle the core material faces is its crush resistance. The compressive loads from attaching bolts would likely be orders of

magnitude above typical compressive strengths of common core materials such as balsa wood, which has been used in pultrusion processes in the past. For example, the transverse compressive strength of a high density balsa wood designed for use as a core material is only 184 psi [14]. Aramid and aluminum honeycomb compressive strengths can range from 50 to 2900 psi depending on cell size, and cell wall gauge [15]. These issues can be ameliorated with solid fastener inserts, but this greatly increases manufacturing difficulties with the pultrusion process. Due to these factors, a core material in the web of the beam is not feasible.

6.5.3.5 Core Materials in the Flanges

Prototype-B-9 and prorotype-B-10 look at the use of core materials in the flanges under maximum geometry constraints, and the results are favorable but, again, unrealistic. The higher allowable flange thickness allows the use of the spacing effect between the triaxial plies to increase torsional stiffness. This was not possible in the flanges under the preferred geometry constraints. Prototype-B-9 has a web layup of $\left[\text{SM-UD}_4/\text{SM-TA}_2\right]_S$ and a flange layup of $\left[\text{SM-UD}_4/\text{SM-TA}_2/\text{SM-UD}_{8.2}/\text{core}\right]_S$ with a core thickness of 0.17 in. Prototype-B-10 is similar but uses IM unidirectional CFRP instead of SM unidirectional CFRP. Prototype B-10 has a web layup of $\left[\text{IM-UD}_2/\text{SM-TA}_2/\text{IM-UD}\right]_S$ and a flange layup of $\left[\text{IM-UD}_2/\text{SM-TA}_2/\text{IM-UD}_{7.5}/\text{core}\right]_S$ with a core thickness of 0.28 in. Prorotype-B-9 and prototype-B-10 have the lowest cost per weight-savings of any design so far, with values of 24.0 and 22.7, respectively.

Again, these favorable results are unrealistic. The core material used in these models has no density and no cost. The additional manufacturing difficulties would also increase manufacturing cost considerably. Having a core in the flanges would also prevent anything from being bolted to the flanges, due to the crush resistance issues described in the previous section. Lastly, the large modulus mismatch between the core material and the surrounding CFRP would create a possible crack initiation point.

6.5.4 Prototype-B Cost Variation

The cost of the prototype-B designs were modeled for a range of material costs. Discussions with the manufacturer revealed a common range for fiber and resins cost. The low and high ends of the range were modeled to see if the manufactured cost ratio per weight saved ratio would reach closer to the target of 13.5. The previous simulations assumed costs near the high end of the range. The manufactured cost ratio versus weight saved ratio range is shown in Figure 25.

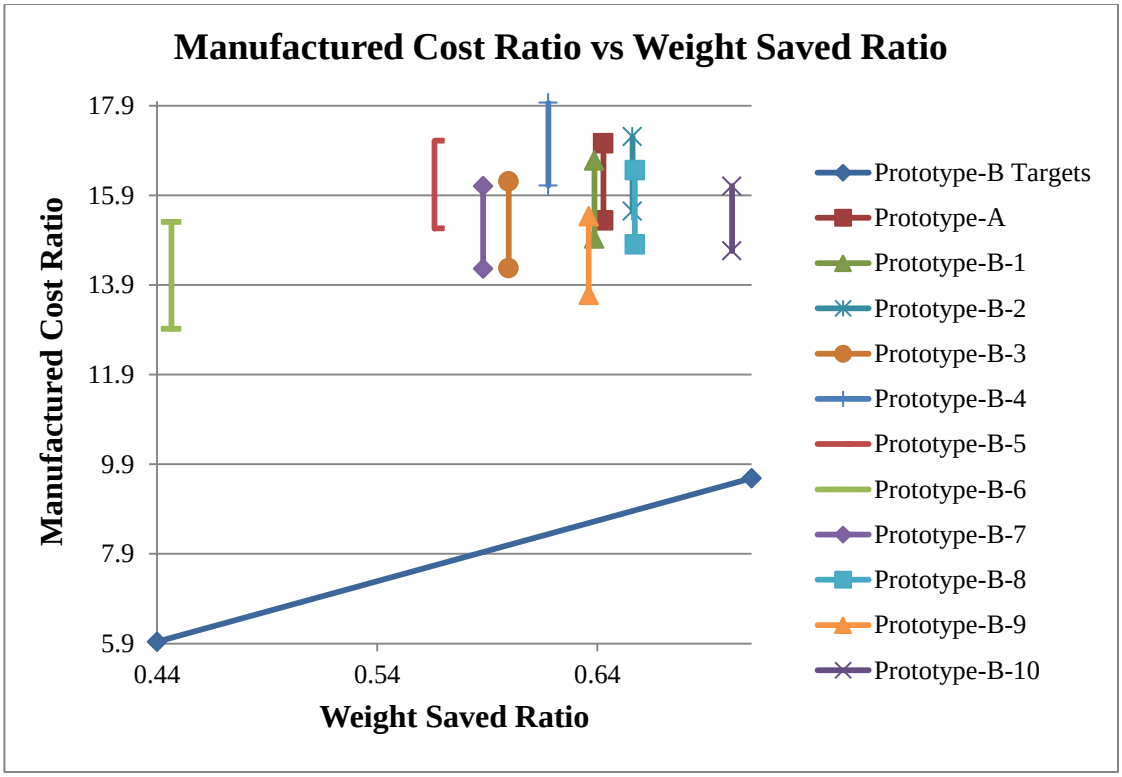

Figure 25 Manufactured cost ratio vs. weight saved ratio range for prototype-B beam designs

The graph shows that even using the lowest end of the material costs does not bring any of the designs close to the target (diagonal line). The better performing designs are lower (lower cost ratio) and further to the right (more weight savings). However, the best performing designs, such as prototype-B-9 and prototype-B-10, do not meet the preferred geometry constraints and used the unrealistic core materials. The best overall design is discussed in the following section.

6.5.5 Prototype-B Design Recommendation

Although none of the prototype-B designs could come close to the desired cost per weight-savings target, prototype-B-2 is the best overall design. It has the second

lowest cost per weight-savings of any design that meets the preferred geometry constraints, and is only 0.55% more expensive than the prototype-B-1 design. It also saves the most weight of any of the four designs, saving 1.73% more weight than prototype-B-1. Meeting the geometry constraints is an important factor in selecting a design, as it prevents any attaching components from having to be modified. Prototype-B-2 does not use any glass fiber which increases the weight of the beam without decreasing the cost. It also does not use a core material which introduces manufacturing and usability issues.

7 Conclusions

The results of this work reveal key information about the feasibility of using FRP to design lightweight structural beams. When designing pultruded FRP beams, it is important to use the most accurate model inputs available. The most important model input is material properties, which depends heavily on the fiber content. The prototype-A beam showed that this value is around 64% by weight for CFRP. It is important to anticipate other defects such as altered geometry due to residual stresses, ply folds, missing plies, and voids. The prototype-A beam revealed that these defects account for about 23% of the stiffness error. This value can be used as a rough estimate when designing new composite beams.

Using what was learned from the prototype-A beam, additional information on material type was revealed during the prototype-B modeling process. The most important information the models showed is that fiberglass is not a viable alternative

to carbon fiber when designing for equivalent stiffness. The prototype-B designs that used fiberglass in unidirectional or triaxial configuration were the worst performing in terms of cost per weight savings. In fact, the amount of fiberglass required to meet the equivalent stiffness of steel weighs more than the steel, which means that fiberglass provides no benefit, despite its lower cost. Standard modulus carbon fiber and intermediate modulus carbon fiber were also compared, with the standard modulus carbon fiber designs usually performing slightly better in terms of cost per weight-savings. However, the cost of materials is likely to vary, so the better performing fiber could change. It is also worth noting that the additional weight savings of the intermediate modulus carbon may be worth the additional cost since lightweighting a structure can be a diminishing returns process. Finally, core materials were shown to give a slight benefit, but only in an ideal case scenario. In reality, the core materials were not feasible, as they would not handle the clamp loads applied by the attaching bolts. Even with this information about ideal materials, the target cost per weight savings ratio could not be reached. The manufactured cost would need to be reduced by almost 50% in order to reach the target.

8 Bibliography

[1] E. J. Barbero, Introduction to Composite Materials Design, Boca Raton: CRC Press, 2011.

[2] J. Faddoul, "Preliminary Evaluation of Fiber Composite Reinforcement of Truck Frame Rails," *SAE Technical Paper,* 1977.

[3] J. Brouhton, A. Beevers and A. Hutchinson, "Carbon-fibre-reinforced plastic (CFRP) strengthening of aluminium extrusions," *Int. J. Adhesion and Adhesives,* vol. 17, pp. 269-278, 1997.

[4] J. Deng, M. Lee and S. Moy, "Stress analysis fo steel beams reinforced with a bonded CFRP plate," *Composite Structures,* vol. 65, pp. 205-215, 2004.

[5] L. Bank, "Flexural and Shear Moduli of Full-Section Fiber Reinforced Plastic (FRP) Pultruded Beams," *Journal of Testing and Evaluation,* vol. 17, no. 1, pp. 40-45, 1989.

[6] R. J. Brooks and G. J. Turvey, "Lateral buckling of pultruded GRP I-section cantilevers," *Composite Structures,* vol. 32, pp. 203-215, 1995.

[7] J. Davalos, H. Salim, P. Qiao and R. Lopez-Anido, "Analysis and design of pultruded FRP shapes under bending," *Composites: Part B,* vol. 27B, pp. 295-305, 1996.

[8] J. Davalos and P. Qiao, "Analytical and Experiemntal Study of Lateral and Distortional Buckling of FRP Wide-Flage Beams," *Journal of Composites for Construction,* pp. 150-159, 1997.

[9] L. Shan and P. Qiao, "Flexural-torsional buckling of fiber-reinforced plastic composite open channel beams," *Composite Structures,* vol. 68, pp. 211-224, 2005.

[10] G. Zhou and J. Hood, "Design, manufacture and evaluation of laminated carbon/epoxy I-beams in bending," *Composites: Part A,* vol. 37, pp. 506-517, 2006.

[11] P. Kim, "A Comparative Study of the Mechanical Performance and Cost of Metal, FRP, and Hybrid Beams," *Applied Composite Materials,* vol. 5, pp. 175-187, 1998.

[12] R. G. B. Warren C. Young, Roark's Formulas for Stress and Strain, New York: McGraw-Hill, 2002.

[13] B. Strong, Fundamentals of Composites Manufacturing, Dearborn: Society of Manufacturing Engineers, 2008.

[14] Gurit, "Balsa Wood Core Material - balsaflex End Grain Balsa," [Online]. Available: http://www.gurit.cm/Files/Documents/Wind%Energy%20Datasheets%20(English)/Balsaflex_WE_v3.pdf. [Accessed 21 August 2012].

[15] Hexcel Composites, "HexWeb Honeycomb Attributes and Properties," 1999. [Online]. Available: http://www.hexcel.com/Resources/DataSheets/Brochure-Data-Sheets/Honeycomb_Attributes_and_Properties.pdf. [Accessed 21 August 2012].

APPENDIX A – MTLB Based MATLAB Program Code

```
%William Koski
%Stiffness calculator for matching FRP beam stiffness to FEA. No
weight or cost calculations.

clear
clc
close all

%% Material Property Calculations

%Lamina properties SM unidirectional CFRP using ROM (Wf = 72.4%)
athk = 0.05;
E11a = 21.9E6;
E22a = 1.16E6;
G12a = 0.616E6;
v12a = 0.253;
v21a = E22a/E11a*v12a;

%Compliance matrix tensor, local coordinates
a = [1/E11a,(-v21a/E22a - v12a/E11a)/2,0;
    (-v12a/E11a - v21a/E22a)/2,1/E22a,0;
    0,0,1/(2*G12a)];
a(4,3) = athk;

%Lamina properties (steel)
Esteel = 29E6;
vsteel = 0.29;
E11s = Esteel;
E22s = Esteel;
G12s = 11.5E6;
v12s = vsteel;
v21s = E22s/E11s*v12s;

%Compliance matrix tensor, local coordinates, steel
s = [1/E11s,(-v21s/E22s - v12s/E11s)/2,0;
    (-v12s/E11s - v21s/E22s)/2,1/E22s,0;
    0,0,1/(2*G12s)];
s(4,1) = 0.284;
s(4,2) = 10;

%%

%Enter plies here (outer to middle, will be symmetric): (need at
least 2)
matltemp(:,:,:,1) = cat(3,a,a,a,a,a);
midplycount = 0;

%%
```

```
%Build full material array
matl =
cat(3,matltemp,flipdim(matltemp(:,:,1:(length(matltemp(1,1,:))-
1)),3));

%Ply thickness array
for q = 1:(length(matl(1,1,:))-1)/2
    plythktemp(q) = matl(4,3,q);
end

plythk =
[cat(2,plythktemp,matl(4,3,(length(matl(1,1,:))+1)/2)*1.000000*midply
count,flipdim(plythktemp,2));
cat(2,plythktemp,matl(4,3,(length(matl(1,1,:))+1)/2)*0.958039*midplyc
ount,flipdim(plythktemp,2));
cat(2,plythktemp,matl(4,3,(length(matl(1,1,:))+1)/2)*0.829795*midplyc
ount,flipdim(plythktemp,2));
cat(2,plythktemp,matl(4,3,(length(matl(1,1,:))+1)/2)*0.643166*midplyc
ount,flipdim(plythktemp,2));
cat(2,plythktemp,matl(4,3,(length(matl(1,1,:))+1)/2)*0.432890*midplyc
ount,flipdim(plythktemp,2));
cat(2,plythktemp,matl(4,3,(length(matl(1,1,:))+1)/2)*0.210765*midplyc
ount,flipdim(plythktemp,2));
cat(2,plythktemp,matl(4,3,(length(matl(1,1,:))+1)/2)*0.049282*midplyc
ount,flipdim(plythktemp,2));
cat(2,plythktemp,matl(4,3,(length(matl(1,1,:))+1)/2)*0.000000*midplyc
ount,flipdim(plythktemp,2))];

%There are 8 diff laminates. Flange, rad6-rad1, Web
numseg = 15;                                %number of segments for
cross-section
lamthk = sum(plythk,2)';            %laminate thicknesses
lamthkfull = cat(2,lamthk,flipdim(lamthk(1:7),2));
numlam = length(plythk(:,1));       %number of laminates
numplies = length(plythk(1,:));     %number of plies per laminate

%%

%Make 3D compliance array (each "page" is the material properties for
each ply)
S12 = matl(1:3,:,:,:);        %complaince matrix of each ply
density = matl(4,1,:,:);      %density of each ply
cost = matl(4,2,:,:);         %cost of each ply
numbeam = length(matl(1,1,1,:));      %number of beam combinations

%Ply angle vectors. Same for each laminate
%plyangdeg = zeros(1,numplies);
plyangdeg = [0,45,-45,90,0,90,-45,45,0];
plyang = plyangdeg*pi/180;          %total ply layup angles (radians)

%Angle of each segment to horizonta
```

```
segangle =
[0,7.5,22.5,37.5,52.5,67.5,82.5,90,97.5,112.5,127.5,142.5,157.5,172.5
,180]*pi/180;   %segment angles (radians)

yia = [4.8,4.788074,4.741183,4.650596,4.522487,4.365587,4.190587,0,-
4.190587,-4.365587,-4.522487,-4.650596,-4.741183,-4.788074,-4.8];
%area cen
bi =
[2.6,0.182737,0.182737,0.182737,0.182737,0.182737,0.182737,8.2,0.1827
37,0.182737,0.182737,0.182737,0.182737,0.182737,2.6];  %segment width
(in)
xia1 =
[2,0.609413,0.434413,0.277513,0.149404,0.058817,0.011926,0,0.011926,0
.058817,0.149404,0.277513,0.434413,0.609413,2];       %segment center
w.r.t. origin

xoffset = sum(xia1.*bi.*lamthkfull)/sum(bi.*lamthkfull);
xia = xia1 - (xoffset); %+lamthk(8)/2);

%Invert plythk matrix, and append it to plythk (to make a fully
symmetric C-channel)
plythkflip = flipdim(plythk(1:7,:),1);
plythk = cat(1,plythk,plythkflip);

%Term scaling matrix to go from tensor to engr definition
termscale = [1,1,1;1,1,1;2,2,2];

%Preallocate arrays
Qo = zeros(3,3,numplies);
z = zeros(1,numplies);
h = zeros(1,numplies);
rearr = zeros(4,4);
redinvj = zeros(4,4,numlam);
EIxglobalsum = zeros(1,numbeam);
EIxeffective = zeros(1,numbeam);
EIyglobalsum = zeros(1,numbeam);
GJrglobalsum = zeros(1,numbeam);
EIxyglobalsum = zeros(1,numbeam);
beamweight = zeros(1,numbeam);
beamcost = zeros(1,numbeam);
segweight = zeros(numseg,numbeam);
segcost = zeros(numseg,numbeam);
plyweight = zeros(numseg,numplies,numbeam);
plycost = zeros(numseg,numplies,numbeam);
plyvol = zeros(numseg,numplies,numbeam);

for n = 1:numbeam

    for j = 1:numlam

        A = zeros(3,3);
        B = zeros(3,3);
```

```
        D = zeros(3,3);

        z(1) = (-lamthk(j)/2) + plythk(j,1);    %z position of top of
ply
        h(1) = ((-lamthk(j)/2) + z(1))/2;       %z position of center
of ply

        for m = 2:numplies
            z(m) = z(m-1) + plythk(j,m);
            h(m) = (z(m) + z(m-1))/2;
        end

        th = plythk(j,:).*h;                                %ply
thickness times z position
        th2 = plythk(j,:).*h.^2 + plythk(j,:).^3/12;    %more math to
make matrix math easier

        for k = 1:numplies
            %Make transformation matrix
            T =
[cos(plyang(k))^2,sin(plyang(k))^2,2*cos(plyang(k))*sin(plyang(k));
            sin(plyang(k))^2,cos(plyang(k))^2,-
2*cos(plyang(k))*sin(plyang(k));
            -
cos(plyang(k))*sin(plyang(k)),cos(plyang(k))*sin(plyang(k)),cos(plyan
g(k))^2-sin(plyang(k))^2];

            %Make compliance matrix tensor, global coords
            Sxyten = T^(-1)*S12(:,:,k,n)*T;
            Sxyeng = Sxyten.*termscale;

            %Invert Sxyeng
            Qo(:,:,k) = Sxyeng^(-1);

            %Generate A, B, D matrices
            A = Qo(:,:,k)*plythk(j,k) + A;
            B = Qo(:,:,k)*th(k) + B;
            D = Qo(:,:,k)*th2(k) + D;
        end

        %Combine to form ABBD matrix, invert to get abbd matrix
        ABBD = [A,B;B,D];
        abbd = ABBD^(-1);

        %reduce and rearrange, then invert it
        rearr(1,1) = abbd(1,1); rearr(1,2) = abbd(1,4);
        rearr(2,1) = abbd(1,4); rearr(2,2) = abbd(4,4);
        rearr(3,3) = abbd(3,3); rearr(3,4) = abbd(3,6);
        rearr(4,3) = abbd(3,6); rearr(4,4) = abbd(6,6);
        redinvj(:,:,j) = rearr^(-1);        %reduced stiffness matrix

    end
```

```
    %Get approximate shear stiffness
    gxy = redinvj(3,3,8)/lamthk(8);
    GA(n) = gxy*bi(8)*lamthk(8);

    %Invert redinv matrix, and append it to redinv (to make a fully
symmetric C-channel)
    redinvjflip = flipdim(redinvj(:,:,1:7),3);
    redinv = cat(3,redinvj,redinvjflip);

    %Preallocate vectors
    Ai = zeros(1,numseg); Bi2 = zeros(1,numseg);
    Ci = zeros(1,numseg); Di = zeros(1,numseg);
    Fi = zeros(1,numseg); Hi = zeros(1,numseg);
    Hibar = zeros(1,numseg);
    ebi = zeros(1,numseg); eqi = zeros(1,numseg);
    DiBar = zeros(1,numseg);
    axialstiff = zeros(1,numseg);
    EIs = zeros(1,numseg);
    EIr = zeros(1,numseg);
    EIx = zeros(1,numseg);
    EIy = zeros(1,numseg);
    EIxy = zeros(1,numseg);
    ESx = zeros(1,numseg);  ESy = zeros(1,numseg);
    px = zeros(1,numseg); py = zeros(1,numseg);
    EIxglobal = zeros(1,numseg);
    EIyglobal = zeros(1,numseg);
    EIxyglobal = zeros(1,numseg);
    GJrglobal = zeros(1,numseg);

    for i = 1:numseg
        Ai(i) = redinv(1,1,i); Bi2(i) = redinv(2,1,i);   %Assign
variables from reduced, inverted
        Ci(i) = redinv(4,3,i); Di(i) = redinv(2,2,i);
        Fi(i) = redinv(3,3,i); Hi(i) = redinv(4,4,i);
        ebi(i) = Bi2(i)/Ai(i);
        eqi(i) = Ci(i)/Fi(i);
        Hibar(i) = Hi(i) - eqi(i)^2*Fi(i);
        DiBar(i) = Di(i) - ebi(i)^2;
        axialstiff(i) = Ai(i)*bi(i);
        EIs(i) = DiBar(i)*bi(i);
        EIr(i) = Ai(i)*bi(i)^3/12;
        EIx(i) = EIs(i)*cos(segangle(i))^2 +
EIr(i)*sin(segangle(i))^2;
        EIy(i) = EIs(i)*sin(segangle(i))^2 +
EIr(i)*cos(segangle(i))^2;
        EIxy(i) = (EIr(i) -
EIs(i))*sin(segangle(i))*cos(segangle(i));
        px(i) = xia(i) - ebi(i)*sin(segangle(i));
        py(i) = yia(i) + ebi(i)*cos(segangle(i));
        ESx(i) = py(i)*axialstiff(i);
        ESy(i) = px(i)*axialstiff(i);
```

```
    end

    axialstiffsum = sum(axialstiff);
    ESxsum = sum(ESx);
    ESysum = sum(ESy);
    xoff = ESysum/axialstiffsum;    %offset to calculate mechanical
centroid x
    yoff = ESxsum/axialstiffsum;    %offset to calculate mechanical
centroid y
    xim = xia - xoff;               %mechanical centroid x
    yim = yia - yoff;               %mechanical centroid y

    for i = 1:numseg
        EIxglobal(i) = EIx(i) + Ai(i)*bi(i)*(yim(i) +
ebi(i)*cos(segangle(i)))^2;
        EIyglobal(i) = EIy(i) + Ai(i)*bi(i)*(xim(i) +
ebi(i)*sin(segangle(i)))^2;
        EIxyglobal(i) = EIxy(i) + Ai(i)*bi(i)*(yim(i) +
ebi(i)*cos(segangle(i)))*(xim(i) - ebi(i)*sin(segangle(i)));
        GJrglobal(i) = Hibar(i)*bi(i);
    end

    EIxglobalsum(n) = sum(EIxglobal);           %vertical bending
siffness
    EIyglobalsum(n) = sum(EIyglobal);           %horizontal bending
stiffness
    GJrglobalsum(n) = 4*sum(GJrglobal);         %torsional bending
stiffness
    EIxeffective(n) = 100^2/(100^2/EIxglobalsum(n) + 3/GA(n));
%effective vertical bending stiffness

end

%Plot centers of beam segments
plot(xia1,yia,'k.')
axis([-1,4,-7,7])
axis equal

hold on

%Plot segments of beam as boxes, with lines along contour
box1x = xia1 + (bi/2).*cos(segangle) + (lamthkfull/2).*sin(segangle);
box1y = yia + (bi/2).*sin(segangle) - (lamthkfull/2).*cos(segangle);
box2x = xia1 + (bi/2).*cos(segangle) - (lamthkfull/2).*sin(segangle);
box2y = yia + (bi/2).*sin(segangle) + (lamthkfull/2).*cos(segangle);
box3x = xia1 - (bi/2).*cos(segangle) - (lamthkfull/2).*sin(segangle);
box3y = yia - (bi/2).*sin(segangle) + (lamthkfull/2).*cos(segangle);
box4x = xia1 - (bi/2).*cos(segangle) + (lamthkfull/2).*sin(segangle);
box4y = yia - (bi/2).*sin(segangle) - (lamthkfull/2).*cos(segangle);
line1x = xia1 + (bi/2).*cos(segangle);
line1y = yia + (bi/2).*sin(segangle);
line2x = xia1 - (bi/2).*cos(segangle);
```

```
line2y = yia - (bi/2).*sin(segangle);

for p = 1:numseg

plot([box1x(p),box2x(p),box3x(p),box4x(p),box1x(p)],[box1y(p),box2y(p
),box3y(p),box4y(p),box1y(p)],'k')
    plot([line1x(p),line2x(p)],[line1y(p),line2y(p)],'r')

    if p >= 2
        if sqrt((line1x(p)-line2x(p-1))^2 + (line1y(p)-line2y(p-
1))^2) > 0.00001
            fprintf('Check contour continuity between segments %u and
%u.\r',p-1,p)
        end
    end

end

OuterHeight = box2y(1)-box3y(15);
InnerHeight = box1y(1)-box4y(15);
OuterWidth = box2x(1)-box2x(8);
FlangeThickness = box2y(1)-box1y(1);
WebThickness = box1x(8)-box2x(8);
```

APPENDIX B – Tensile Specimen Testing Result Plots

Web Specimens

This section reviews the tensile testing results for the five web specimen orientations: 0, 30, 45, 60, and 90°. Each figure shows the stress and strain data for a given specimen orientation. A linear trendline was fit to each set of data, and the equation for each trendline is displayed on the plots. The slope of the trendline represents the overall stiffness of each specimen.

Figure 26 shows the stress vs. strain plot for the six 0° web specimens. The average stiffness of the 0° specimens is $7.58*10^6$ psi.

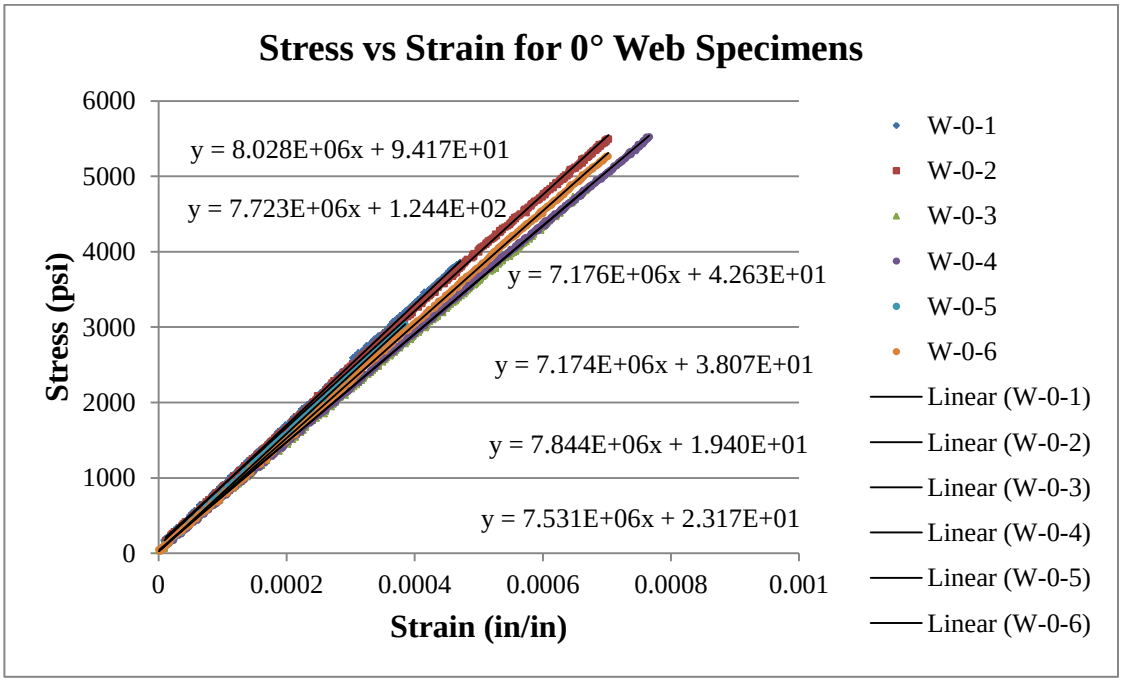

Figure 26 Stress vs. strain plot for 0° web specimens

Figure 27 shows the stress vs. strain plot for the three 30° web specimens. The average stiffness of the specimens is $5.92*10^6$ psi.

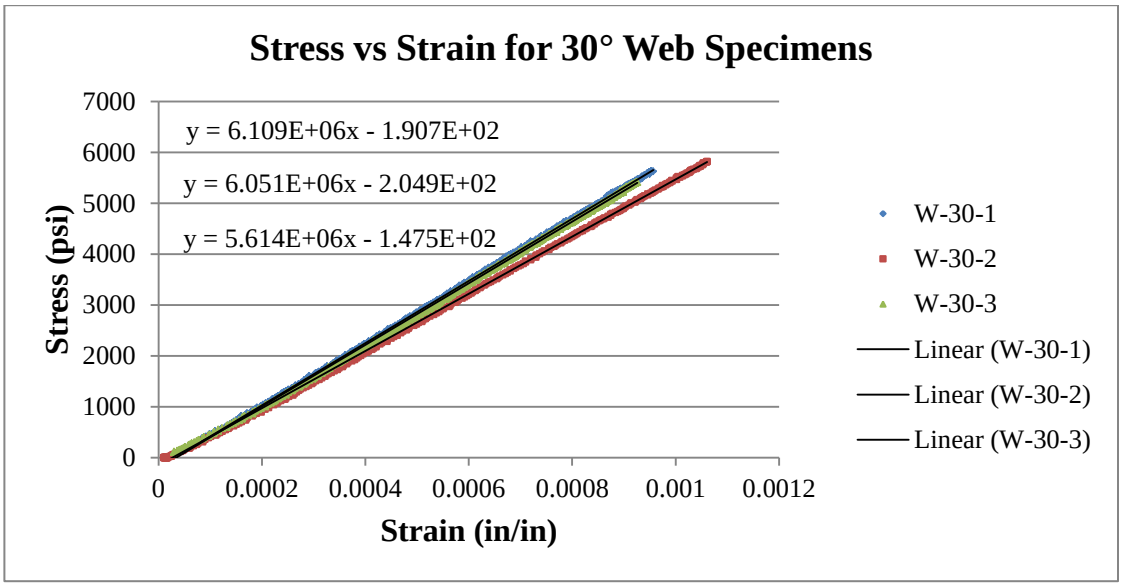

Figure 27 Stress vs. strain plot for 30° web specimens

Figure 28 shows the stress vs. strain plot for the three 45° web specimens. The average stiffness of the specimens is $5.66*10^6$ psi.

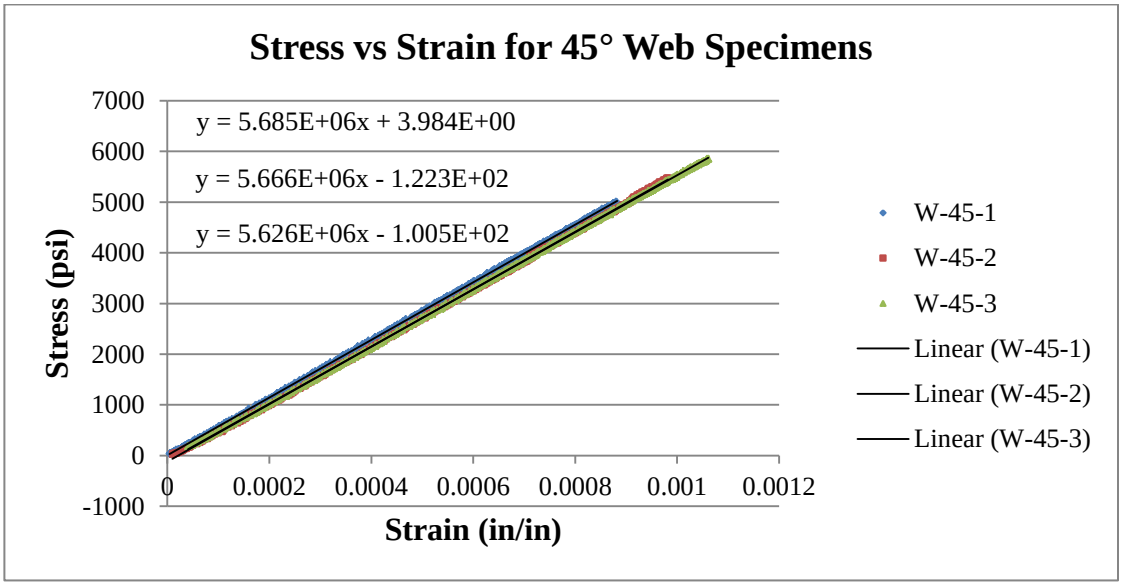

Figure 28 Stress vs. strain plot for 45° web specimens

Figure 29 shows the stress vs. strain plot for the 60° web specimens. The average stiffness of the specimens is $5.65*10^6$ psi.

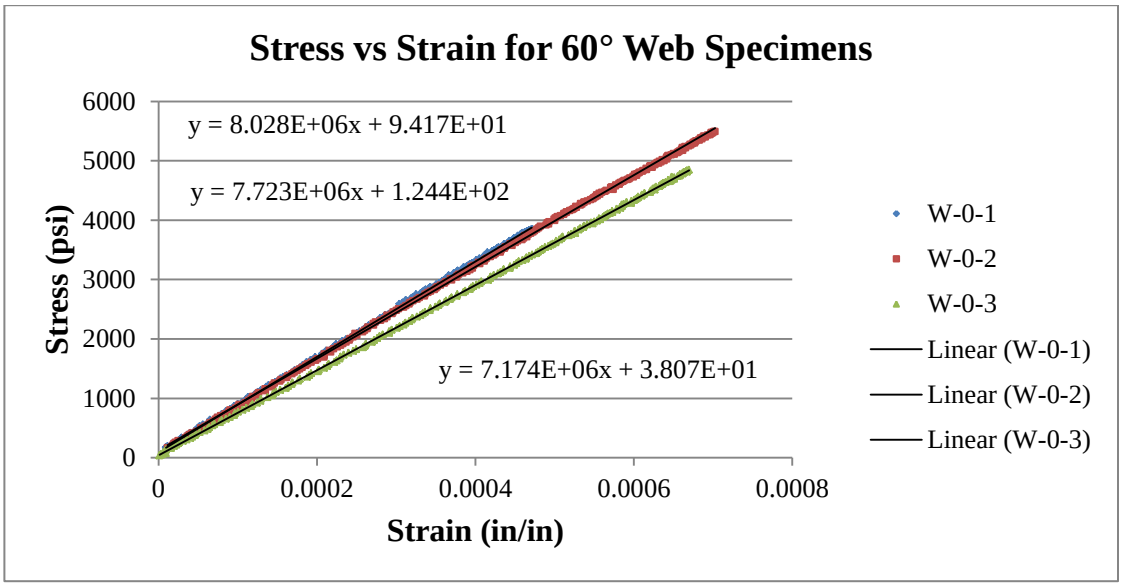

Figure 29 Stress vs. strain plot for 60° web specimens

Figure 30 shows the stress vs. strain plot for the 60° web specimens. The average stiffness of the specimens is $5.71*10^6$ psi.

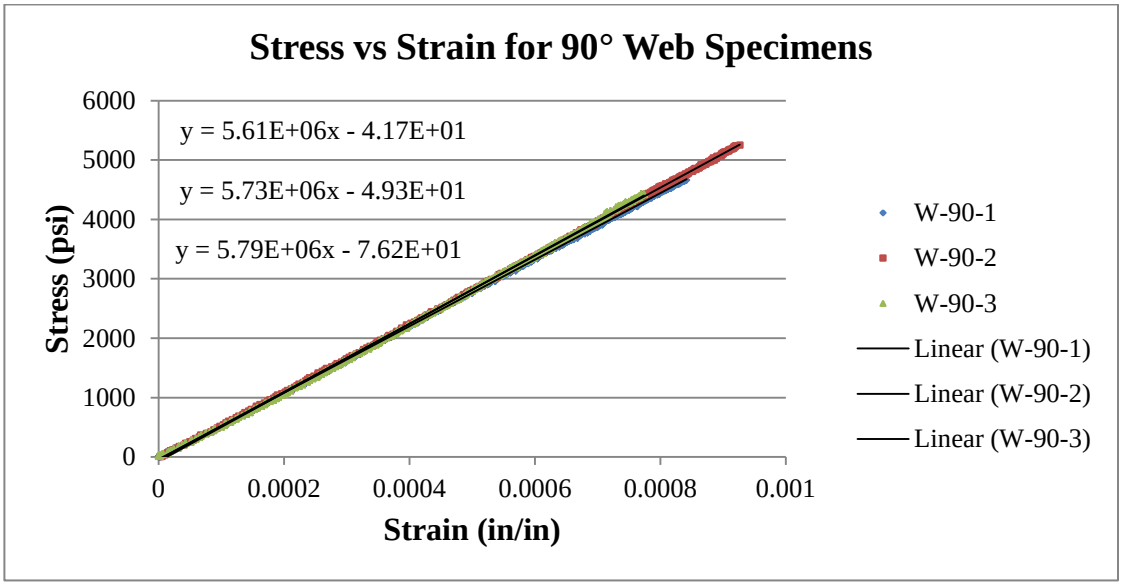

Figure 30 Stress vs. strain plot for 90° web specimens

Flange Specimens

This section reviews the tensile testing results for the two flange specimen orientations: 0 and 15°. Each specimen of each orientation was tested four times. Slight misalignment in the clevis fixture caused uneven loading in the flange specimens. Because of this, each specimen was tested twice with the extensometer clipped on one face and twice more with the extensometer clipped on the opposite face. The face with the painted on specimen label is called "paint side," and the side without the label is called "clean side." The uneven loading caused the beginning of each data set to be curved, so the curved portions were removed from the data. Eventually the loading become more evenly distributed throughout the specimen, and the data became roughly linear. A linear trendline was fit to each set of data, and the equation for each trendline is displayed on the plots. The slope of the trendline represents the overall stiffness of the specimen.

Figure 31 through Figure 34 are stress vs. strain plots for each 0° flange specimen. Specimen F-0-2 was not tested due to cracking that occurred during drilling of the specimen. Specimens F-0-1 and F-0-5 had the missing unidirectional plies described earlier. The average stiffness of the specimens is $1.57*10^7$ psi.

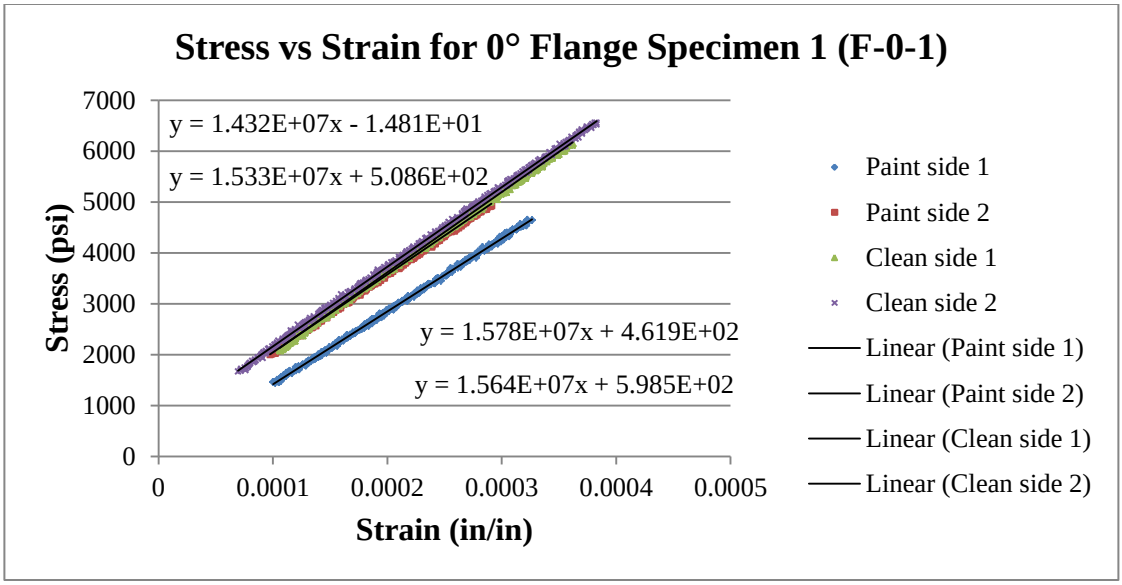

Figure 31 Stress vs. strain plot for 0° flange specimen 1 (F-0-1)

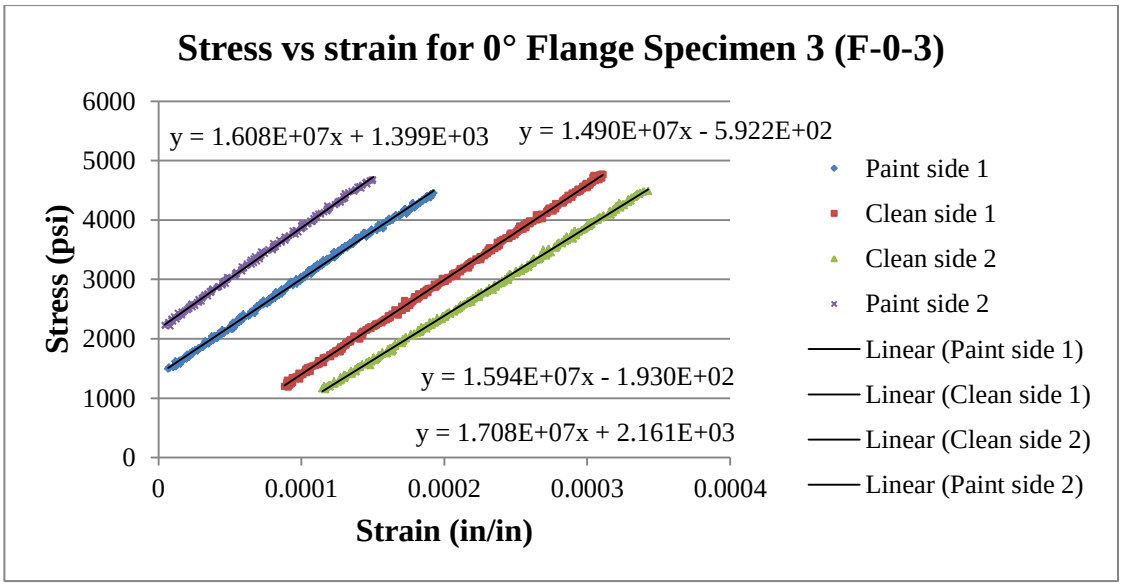

Figure 32 Stress vs. strain plot for 0° flange specimen 3 (F-0-3)

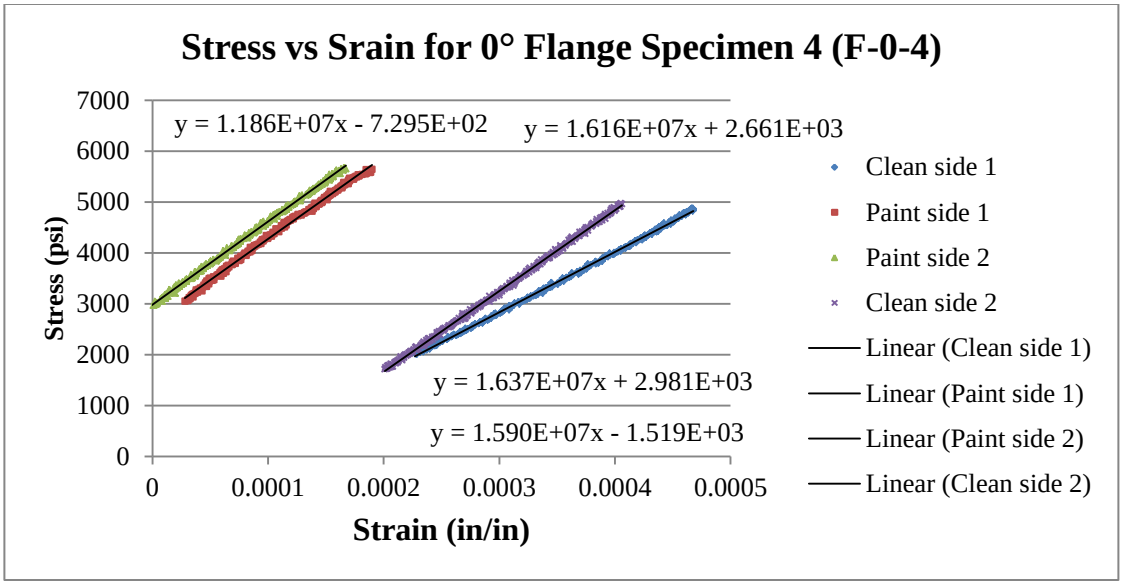

Figure 33 Stress vs. strain plot for 0° flange specimen 4 (F-0-4)

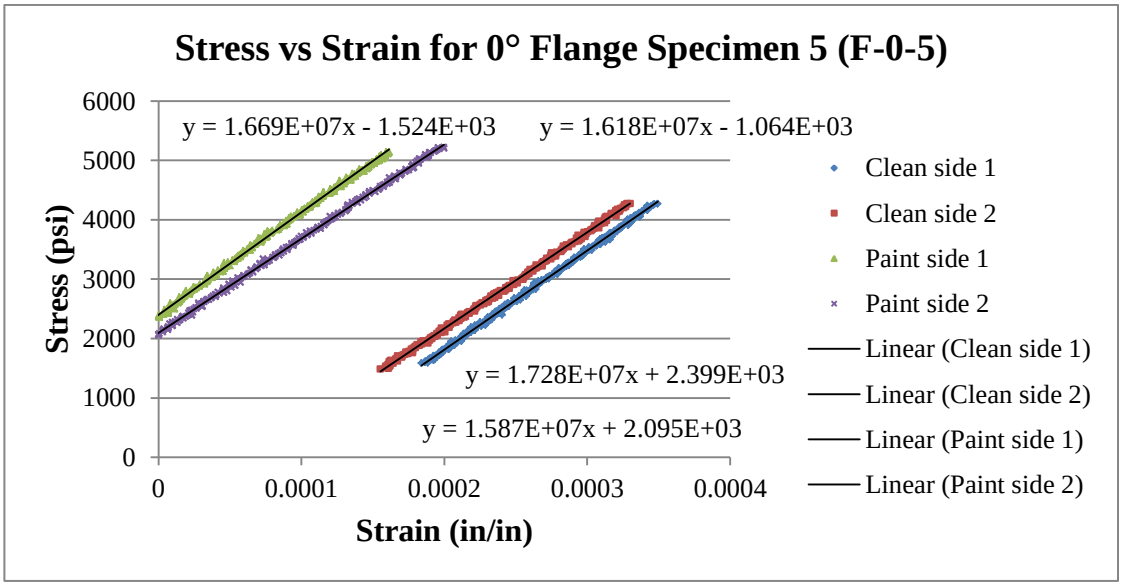

Figure 34 Stress vs. strain plot for 0° flange specimen 5 (F-0-5)

Figure 35 through Figure 39 are stress vs. strain plots for each 15° flange specimen. Specimens F-15-2 and F-15-3 had the missing unidirectional plies described earlier. The average stiffness of the specimens is $8.76*10^6$ psi.

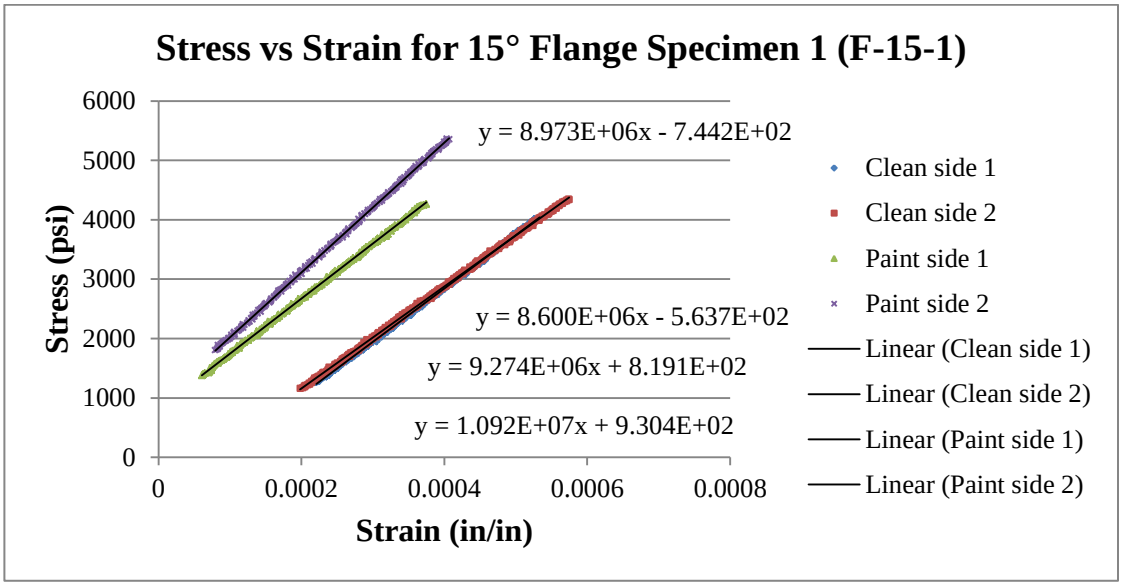

Figure 35 Stress vs. strain plot for 15° flange specimen 1 (F-15-1)

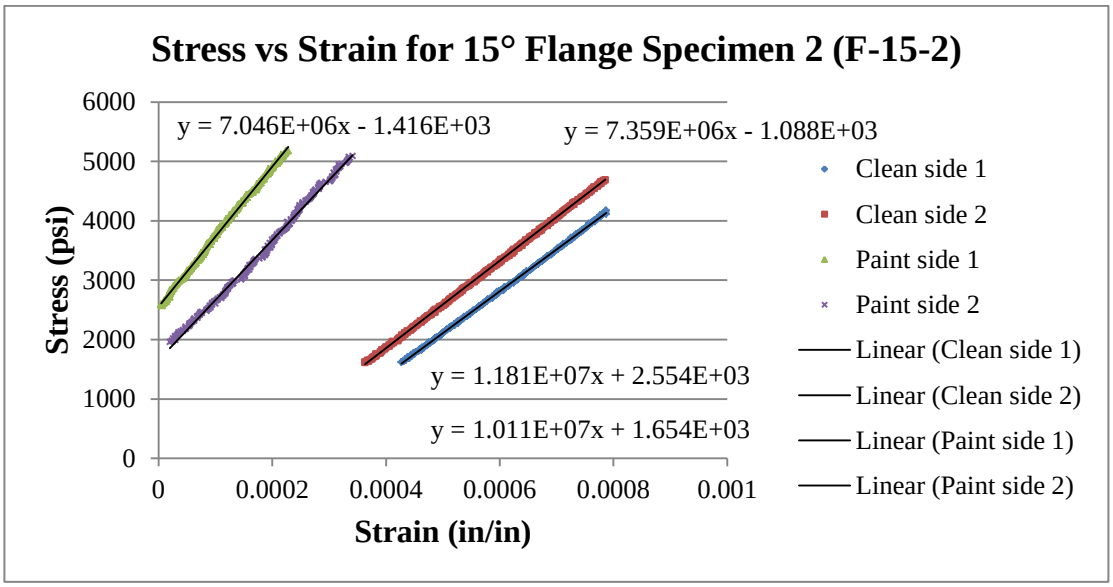

Figure 36 Stress vs. strain plot for 15° flange specimen 2 (F-15-2)

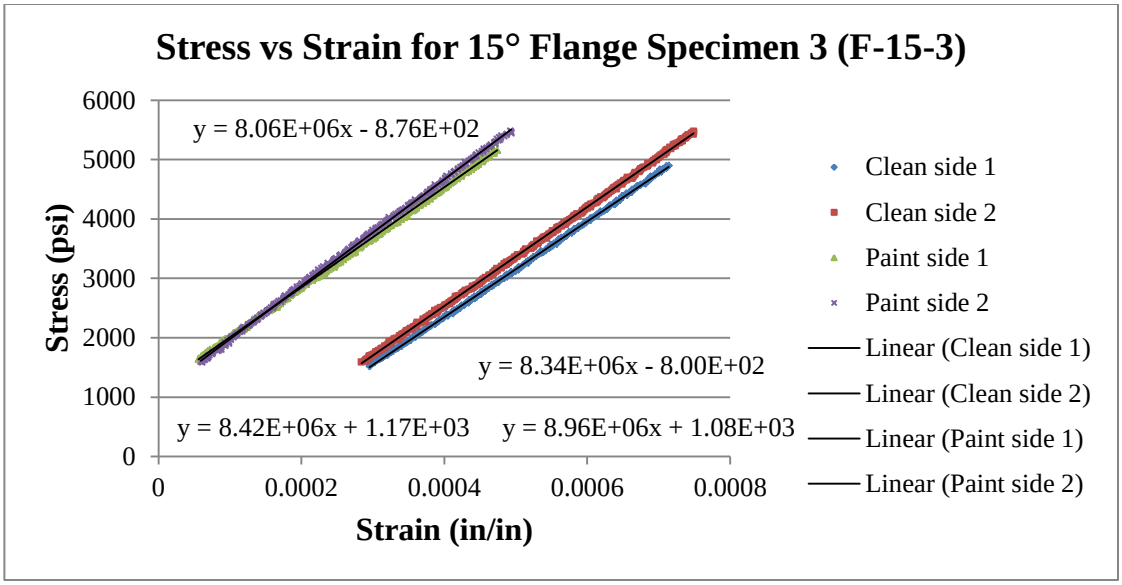

Figure 37 Stress vs. strain plot for 15° flange specimen 3 (F-15-3)

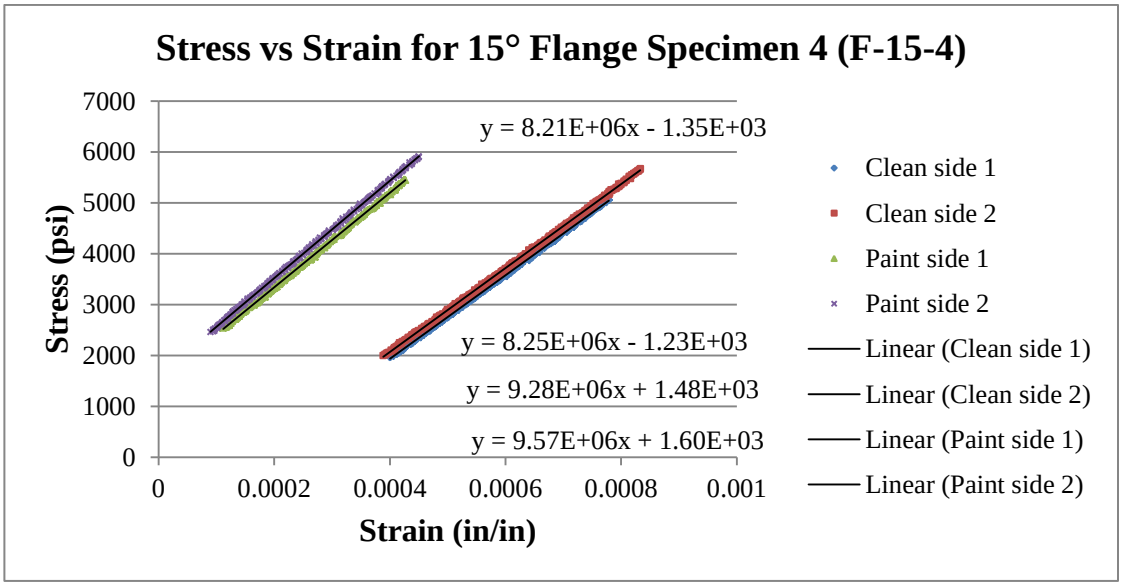

Figure 38 Stress vs. strain plot for 15° flange specimen 4 (F-15-4)

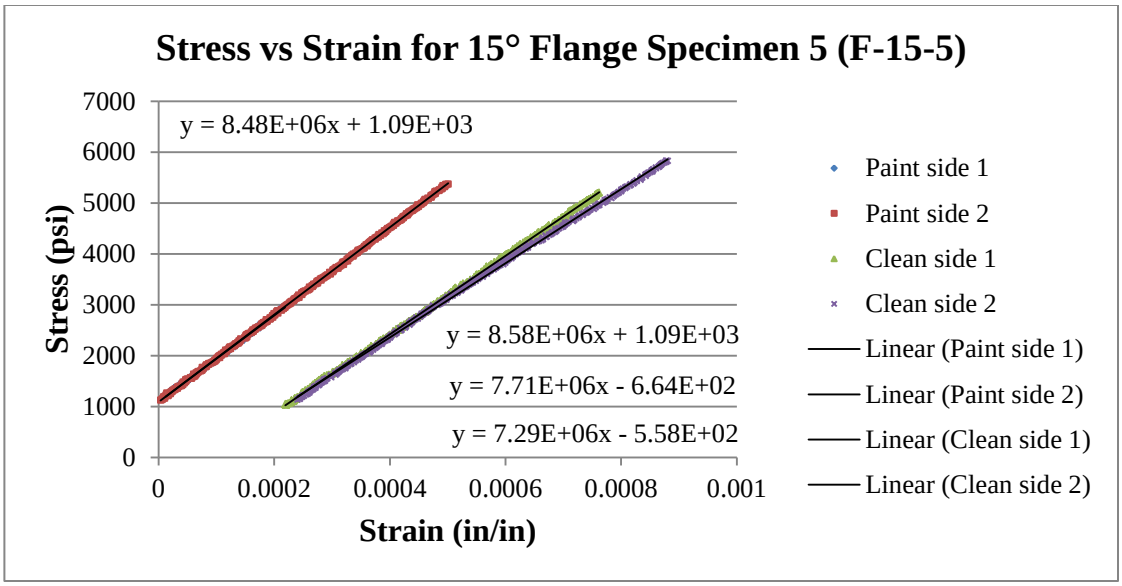

Figure 39 Stress vs. strain plot for 15° flange specimen 5 (F-15-5)